

The High-Resolution Carbon Geography of Perú

A Collaborative Report of the
Carnegie Airborne Observatory and
the Ministry of Environment of Perú

CARNEGIE
INSTITUTION FOR
SCIENCE



Contributors

Gregory P. Asner¹, David E. Knapp¹, Roberta E. Martin¹, Raul Tupayachi¹, Christopher B. Anderson¹, Joseph Mascaro¹, Felipe Sinca¹, K. Dana Chadwick¹, Sinan Sousan¹, Mark Higgins¹, William Farfan², Miles R. Silman², William Augusto Llacayo León³, Adrian Fernando Neyra Palomino³

¹Department of Global Ecology and the Carnegie Airborne Observatory, Carnegie Institution for Science, Stanford, CA USA

²Department of Biology, Wake Forest University, Winston-Salem, NC USA

³Dirección General de Ordenamiento Territorial, Ministerio del Ambiente, San Isidro, Lima, Perú



This project was made possible through a collaboration between the Peruvian Ministry of Environment and the Carnegie Institution for Science.

This conservation, land-use and climate change project was supported by the John D. and Catherine T. MacArthur Foundation, Gordon and Betty Moore Foundation, and the Carnegie Institution for Science.

The Carnegie Airborne Observatory is made possible through the support of the Avatar Alliance Foundation, Grantham Foundation for the Protection of the Environment, John D. and Catherine T. MacArthur Foundation, Gordon and Betty Moore Foundation, W. M. Keck Foundation, Margaret A. Cargill Foundation, Mary Anne Nyburg Baker and G. Leonard Baker Jr., and William R. Hearst III.

MacArthur
Foundation

GORDON AND BETTY
MOORE
FOUNDATION

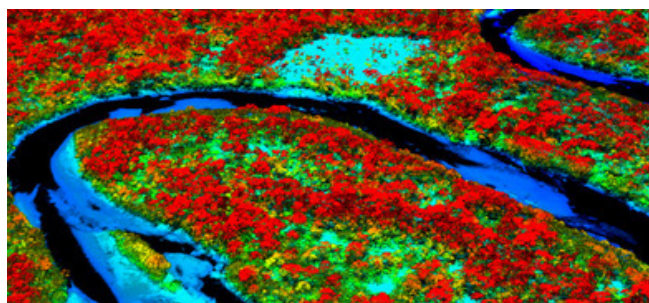


The High-Resolution Carbon Geography of Perú

**A Collaborative Report of the
Carnegie Airborne Observatory and the
Ministry of Environment of Perú**

Table of Contents

Summary	5
Introduction	9
Results and Discussion	13
Conclusions	37
Technical Methodology	39
Appendix	53
Acknowledgments	59
References	61



The Carnegie Airborne Observatory (CAO) was critical to the first-ever mapping of the more than 128 million hectares that comprise the country of Perú. With its all-weather, inter-continental capability, combined with its unique laser and hyperspectral sensors and airborne computing platform, the CAO provided 3-D imaging of Peruvian ecosystems ranging from lowland Amazonian rainforests to high-altitude Andean tundra.

Background

Vegetation is one of the most spatially and temporally dynamic reservoirs of carbon in the world. The amount of carbon stored in vegetation above ground in woody biomass is particularly variable, and is subject to rapid change via land uses that remove vegetation cover, causing carbon emissions. Reducing carbon emissions from deforestation and forest degradation, as well as from other non-forested ecosystems, is therefore a priority in both national and international strategies to conserve ecosystems and to reduce carbon dioxide build-up in the atmosphere.

Perú harbors an enormous range of ecological conditions, from hot and humid lowland Amazonian forests to high-altitude Andean ecosystems and desert conditions on the Pacific coast. The diversity of environments in Perú greatly challenges efforts to measure, map and monitor carbon stocks throughout the country.

Purpose

We report the first high-resolution geographic study of aboveground carbon stocks throughout the more than 128 million hectares that comprise the country of Perú. This report communicates the development of our methodology and an extensive validation of the resulting high-resolution carbon map of Perú. It also provides the first quantitative analysis of the basic environmental factors determining the carbon geography of Peruvian ecosystems, political regions, and protected areas.

Methodology

To create a map of aboveground carbon density (ACD) at one-hectare resolution, we integrated airborne Light Detection and Ranging (LiDAR) technology, a new field plot inventory network, freely available satellite imagery, and geostatistical scaling techniques. Following initial establishment and operationalization of the described methodology, the approach can be readily updated over time to provide a long-term monitoring capability with reported uncertainties for every hectare within Perú.

Performance

Based on an initial environmental stratification of the region, and using the Carnegie Airborne Observatory LiDAR, we sampled 6.7 million hectares of ecosystems distributed in Perú at a resolution of 1.1 meter. To scale these airborne LiDAR samples to the national level, we developed a geostatistical modeling approach based on the well-known Random Forest Machine Learning (RFML) algorithm, which we used with a suite of environmental maps of Perú derived from satellite imagery. The RFML nationwide mapping of vegetation canopy height — a key input to mapping of aboveground carbon density — was validated in 536,874 additional hectares of direct LiDAR measurements distributed throughout the country. This showed that vegetation canopy height could be mapped with a precision of 78% and an error (RMSE) of 3.5 meters at the national level.

We calibrated the mapped canopy height estimates to field-based estimates of aboveground carbon density (ACD; units of Mg C ha⁻¹ or metric tons of C per hectare) across a wide range of vegetation types and land-use conditions. Our field inventory network is comprised of 272 permanent field plots distributed in lowland, submontane and montane ecosystems. Extensive validation procedures show that remotely sensed measurements of vegetation canopy height can be used to estimate the carbon stocks of laboriously hand-measured field plots with an average 11.6% uncertainty. This uncertainty is less than the uncertainty of field-based estimates of carbon stocks.

Findings

The resulting map of aboveground carbon density in Perú reveals a very wide range of ecosystem-level carbon density values, from less than 5 Mg C ha⁻¹ in ultra-dry desert systems on the western, leeward side of the Andes, to more than 150 Mg C ha⁻¹ in the northeastern, humid lowland Amazonian forests. The total estimated aboveground carbon stock of Perú is 6.9223 Pg (billion metric tons).

The median carbon density for all Peruvian forests is 99.3 Mg C ha⁻¹, and the maximum-recorded density is 167.6 Mg C ha⁻¹. More than 50% of all Peruvian forests harbor aboveground carbon densities of more than 100 Mg C ha⁻¹, but only 10% of these exceed 125 Mg C ha⁻¹. The vast majority of these high-biomass forests are located in the lowland and submontane regions of the Amazon, usually below 1000 m elevation.

Aboveground carbon densities and total carbon stocks varied enormously by Peruvian Regional jurisdiction. Loreto contains 53% of Perú's aboveground carbon stock, owing to the large size of this Region and its particularly high carbon densities (98.8 ± 29.4 Mg C ha⁻¹). The second and third largest Regional stocks are found in Ucayali and Madre de Dios, respectively. Combined these two Regions contain 26% of the total Peruvian carbon stock. Other Regions with large stocks include San Martín, Amazonas, Cusco, Junín, Huánuco, Pasco and Puno, although together they comprise just 18.5% of the total aboveground carbon stock of the country.

Other highlights include: (i) The highest carbon stocks of 128 ± 14 Mg C ha⁻¹ are found to the North of the Napo and Amazon rivers, and along the Northeast Peruvian border with the Brazilian state of Amazonas. (ii) In the



Northern lowlands, the Pacaya-Samiria swampland harbors suppressed and highly variable aboveground carbon stocks in the range of $54 \pm 28 \text{ Mg C ha}^{-1}$. (iii) The cities of Tarapoto and Pucallpa are centers of low forest carbon stocks resulting from past deforestation, with Pucallpa being the region of maximum loss throughout the Peruvian Amazonian lowlands. (iv) Additional losses are clearly visible for Iquitos in Loreto, and especially for Puerto Maldonado in Madre de Dios. The latter is closely associated with very large areas of near-zero carbon storage caused by gold mining. (v) The lowlands of southern Perú harbor lower carbon stocks associated with extensive areas of bamboo. (vi) On the Pacific coast of Perú, carbon densities are primarily in the $1\text{-}8 \text{ Mg C ha}^{-1}$ range, with local peaks of $22\text{-}52 \text{ Mg C ha}^{-1}$ in intensively managed woodland plantations.

We assessed the aboveground carbon density and total carbon stocks of 174 protected areas throughout Perú. A total of 1.816 Pg (billion metric tons) of carbon are stored in aboveground vegetation within these protected areas, or about 26% of the total estimated aboveground carbon stocks found within Perú. This leaves up to 74% of aboveground carbon stocks outside of these protected areas. The largest carbon stocks are found in the fifteen largest forest reserves, including the Alto Purus, Manu, Cordillera Azul and Bahuaja Sonene national parks, Pacaya Samiria and Pucacuro national reserves, and the Alto Nanay-Pintuyacu Chambira, Ampiyacu Apayacu, Sierra del Divisor, Yaguas and Santiago Comaina reserves. These protected areas alone comprise 85% of the total aboveground carbon stores among the 174 protected areas that we assessed. Within humid Amazonian and Andean forests, the size of each protected area is highly correlated with its total carbon stock, with each hectare of protection adding an average 95.1 Mg (metric tons) of carbon to the biosphere.

Conclusions

Using a strategic and cost-effective combination of airborne LiDAR sampling, tactically placed field calibration plots, freely available satellite data, and a new geostatistical modeling approach, we have shown that a high-resolution geography of aboveground carbon stocks can be revealed for a large and environmentally complex country such as Perú. This new carbon geography also includes spatially explicit maps of uncertainty, which is essential in decision-making for conservation, management and policy development efforts associated with ecosystems and societal use of lands.

Our effort focused on the mean and uncertainty of aboveground carbon stocks in every hectare of Perú, thereby providing a new basis for all stakeholders, large and small, to participate in improving the use and conservation of ecosystems. The detailed validation presented at multiple steps throughout the study demonstrates that aboveground carbon stocks can be estimated and mapped with a degree of uncertainty that is indistinguishable from laborious hand-measured, field-based estimates. Moreover, the approach presented here is spatially continuous, and thus less prone to error caused by environmental and human-driven variation in carbon stocks. Updates to the carbon map, as well as spatially explicit changes in carbon stocks, will be far easier to implement going forward based on the methodology and base data layers presented in this report.



The international community has championed forest carbon sequestration and emission reductions as a strategy to mitigate climate change¹. In combination, deforestation and forest degradation account for up to 15% of global carbon dioxide emissions to the atmosphere². Yet the geography of forest carbon stocks remains poorly known, which leads to great uncertainty in creating spatially explicit estimates of forest carbon emissions over time³. Large emission uncertainties, in turn, result in financial discounts placed on forest carbon, which then decrease its investment power to combat climate change^{4,5}. This ultimately limits forest carbon sequestration projects to volunteer markets or demonstration activities, mostly implemented at the project or local scale. Future compliance or market-based carbon sequestration agreements will hinge upon accurate, high-resolution monitoring at large geographic scales relevant to a nested set of stakeholders ranging from individual landowners, to jurisdictional agencies, and national governments. The critical resolution for carbon monitoring is the hectare (= 2.5 acres), which is the world's most common unit of land tenure, ownership and regulatory policy⁶. Thus to achieve full accounting the geography of carbon stocks must be known for every hectare in a country.

Beyond the policy-driven need for high-resolution mapping and monitoring of forest carbon stocks, the geography of terrestrial carbon storage is central to our understanding of numerous ecological patterns and processes ranging from habitat and biodiversity distributions, to global carbon cycling and climate-biosphere interactions. Natural tropical forests, for example, store a majority of their aboveground carbon (which is 48% of dry biomass) in large, interlocking tree canopies that also provide critical habitat for many thousands of avian, mammalian and invertebrate species⁷. In contrast, low carbon stocks in natural tropical forests are often indicative of climatic and hydrological limitations to productivity, as well as disturbance-driven mortality of forest canopies^{8,9}. By mapping aboveground carbon stocks at high resolution, critically important processes that determine ecological dynamics and habitat conditions are uniquely revealed.

Numerous factors limit our current understanding of the world's carbon geography. First, the distribution of carbon stocks is highly uneven across the land surface, owing to the complex and interactive effects of abiotic (e.g., climate, soils, geology, topography, hydrology) and biotic (e.g., community composition, human activities) processes¹⁰⁻¹². Field sampling techniques alone, such as with inventory plots, cannot capture the spatial variability of carbon stocks over large regions, and any resulting carbon emission estimates based on field plot data are highly vulnerable to large errors. Second, no current satellite systems provide plot-like

Figure 1 (opposite page)

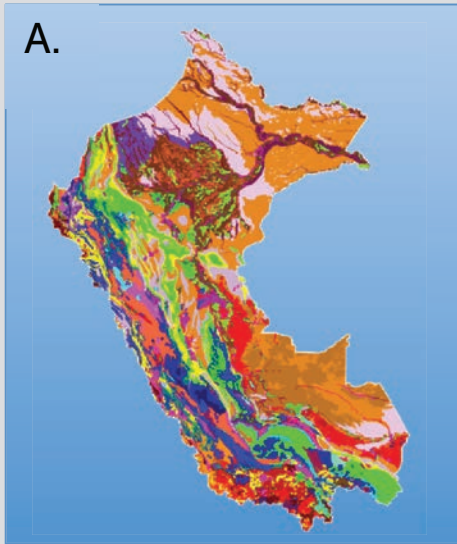
Overview of the methodology used to map vegetation carbon stocks throughout the country of Perú: (A) A pre-stratification step combines geological, soil, community floristic composition, elevation, and forest cover maps to forecast the potential range of environmental conditions to be encountered during airborne surveys. (B) The country is gridded into 100 x 100 km sampling cells, and airborne Light Detection and Ranging (LiDAR) is used to massively sample each grid cell. Over-sampling is achieved by ensuring that large areas are covered for each potential set of environmental conditions estimated during pre-stratification. (C) A diverse array of satellite data is compiled to provide continuous geographic information on vegetation cover, topographic variables, and climate. (D) The satellite and LiDAR data are processed through a geostatistical modeling approach, and combined with calibrations of LiDAR to field-estimated carbon stocks, to map aboveground carbon stocks at one-hectare resolution, along with spatially explicit uncertainty maps.

sampling measurements with sufficient detail to support robust estimates of aboveground carbon stocks at high spatial resolution. As a result, global or pan-tropical carbon maps derived from satellites currently may not agree well with one another¹³, and they may not agree with current sparse distributions of field inventory plots¹⁴. Third, whether sampled with field or remote sensing techniques, the acquired metrics of vegetation structure (e.g., tree height, diameter) require allometric equations to estimate aboveground carbon stocks¹⁵. This process is prone to systematic bias, particularly with respect to floristic controls on carbon stocks, such as crown architecture and wood density¹⁶.

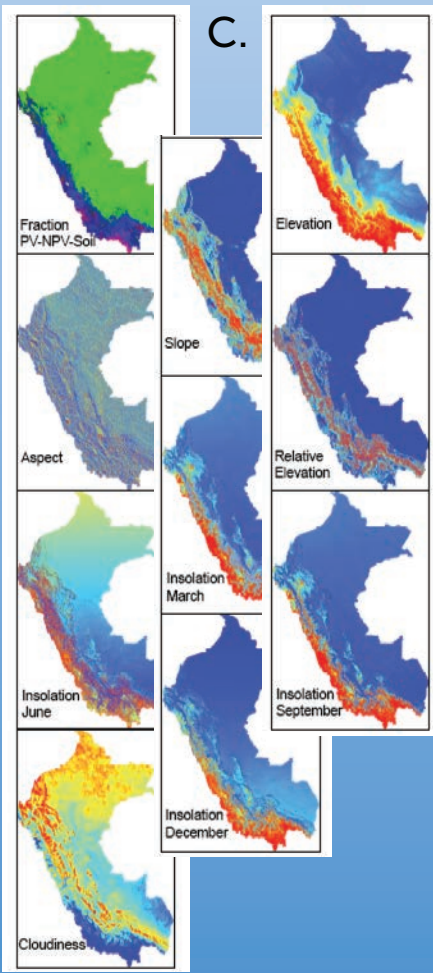
We present the first high-resolution geographic study of aboveground carbon stocks for the country of Perú. Covering a total area of more than 128 million ha, Perú harbors enormous environmental and biological gradients, from the warm lowlands of the Amazonian forest in the east, to the cold montane ecosystems of the Andes. The forested portion of the country covers approximately 68 million ha, making it a core focus of this study. To create a map of aboveground carbon stocks at one-hectare resolution, we integrated and applied a combination of airborne Light Detection and Ranging (LiDAR) technology, freely available satellite imagery, distributed field calibration plots, and geostatistical scaling techniques (**Figure 1**). The methodology, which is explained to detail in the Technical Methodology section of this report, is scalable to any geography and is readily updateable over time. Following the development and extensive validation of the resulting high-resolution carbon map of Perú, we quantify for the first time the relative importance of the environmental factors that fundamentally determine the carbon geography of western Amazonian and Andean ecosystems.

Satellite & GPS Data

A.



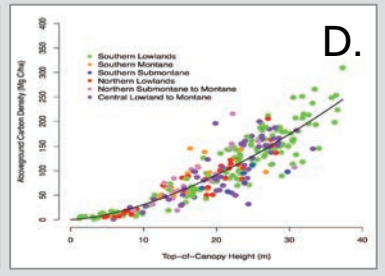
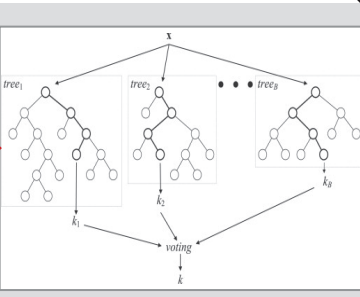
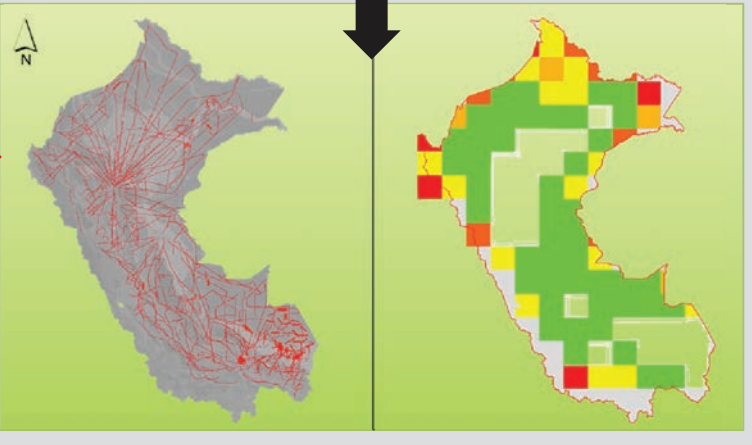
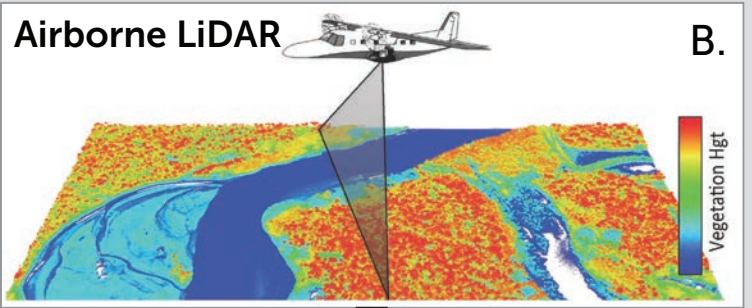
Pre-stratification



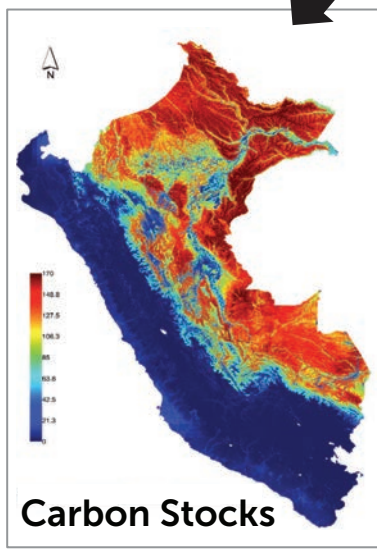
Environmental Mapping

Airborne LiDAR

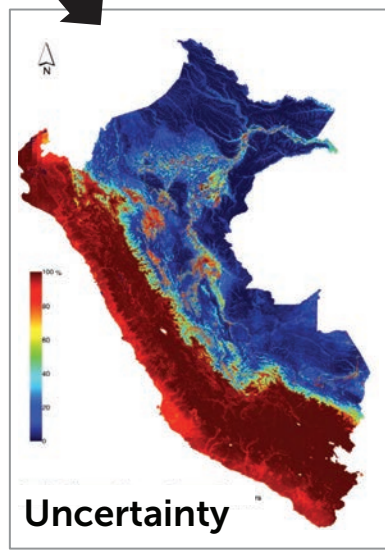
B.



Modeling and Field Plots



Carbon Stocks



Uncertainty

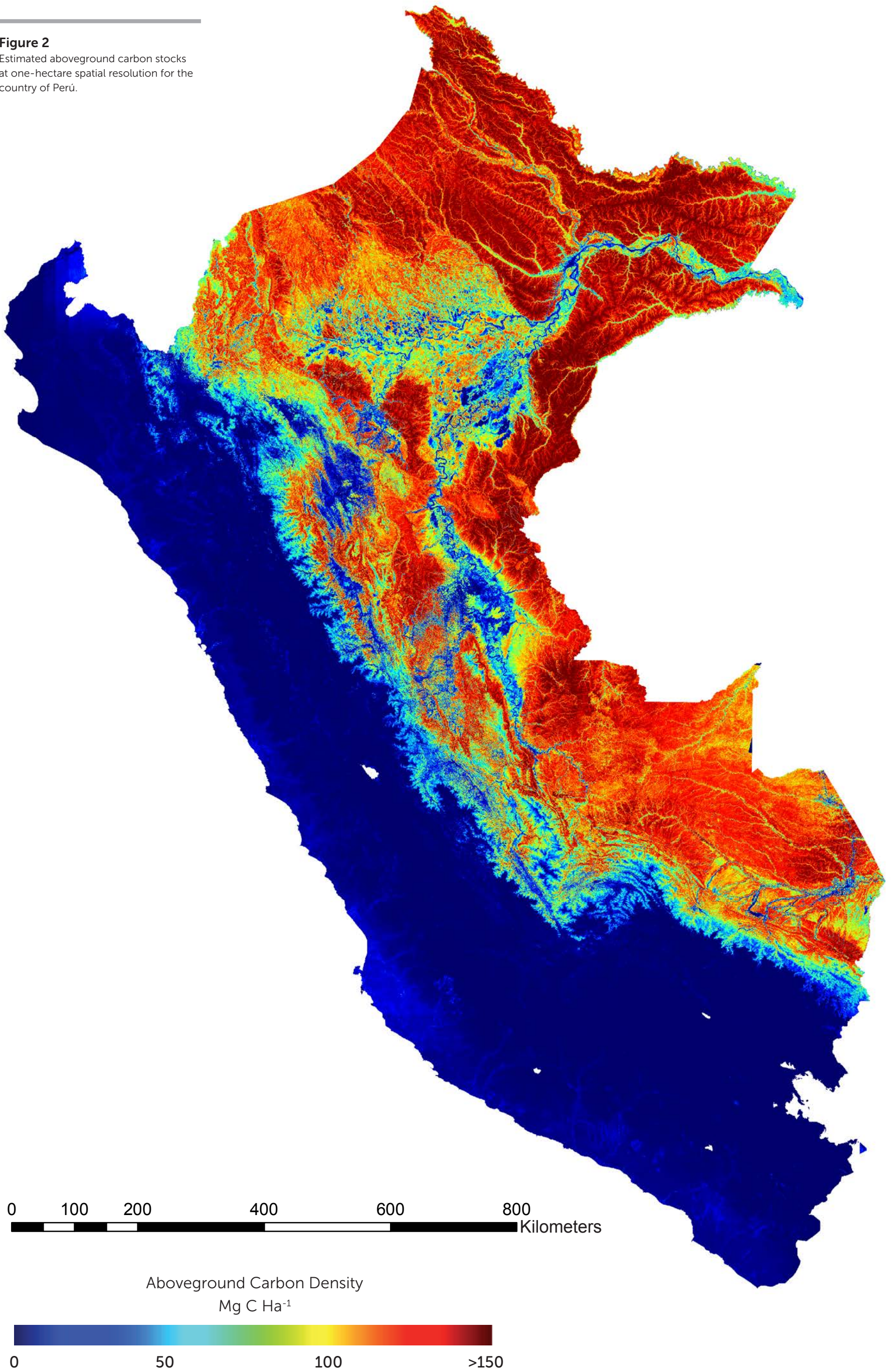
Carbon Geography of Perú

The high-resolution aboveground carbon stock map of Perú is shown in Figure 2 (see fold-out). The map reveals a global range of ecosystem-level carbon density values, from less than 5 Mg C ha⁻¹ in ultra-dry desert systems on the western, leeward side of the Andes, to more than 150 Mg C ha⁻¹ in the northeastern, humid lowland Amazonian forests. The total estimated aboveground carbon stock of Perú is 6.9223 Pg or billion metric tons.

From North to South, the following major features are revealed in this map, as annotated in Appendix Figure S1:

1. The highest carbon stocks of 128 ± 14 Mg C ha⁻¹ are found to the North of the Napo and Amazon rivers, and along the Northeast Peruvian border with the Brazilian state of Amazonas.
2. In the Northern lowlands, carbon stocks are 10-15% higher on the lower-fertility Nauta geologic formations (110 Mg C ha⁻¹) compared to their neighboring Pebas geologic formations (95 Mg C ha⁻¹; see GeoEcoElevation map in the Technical Methodology section).
3. In the Northern lowlands, the Pacaya-Samiria swampland harbors sharply suppressed and highly variable aboveground carbon stocks in the range of 54 ± 28 Mg C ha⁻¹.
4. The transition from the Northern lowland carbon stocks to those found at treeline in the Andes is gradual in comparison to that of the Southern lowlands.
5. The cities of Tarapoto and Pucallpa are centers of lost forest carbon stocks resulting from deforestation, with Pucallpa being the region of maximum loss throughout the Peruvian Amazonian lowlands. Additional losses are clearly visible for Iquitos in Loreto, and especially for Puerto Maldonado in Madre de Dios. The latter is closely associated with very large areas of near-zero carbon storage caused by gold mining¹⁷.
6. The lowlands of southern Perú harbor lower carbon stocks associated with extensive areas of bamboo (90 ± 8 Mg C ha⁻¹).
7. Throughout the upper portion of the Fitzcarrald Arch geologic formation, aboveground carbon stocks vary from high values (101 ± 12 Mg C ha⁻¹) in local valleys to low values (42 ± 10 Mg C ha⁻¹) in crest topographic positions.

Figure 2
Estimated aboveground carbon stocks
at one-hectare spatial resolution for the
country of Perú.



8. On the Pacific coast of Perú, carbon stocks increase to a maximum of 8 ± 2 Mg C ha⁻¹ in the Ica Region south of Lima. Other coastal communities have carbon densities in the 1-8 Mg C ha⁻¹ range, with local peaks of 22-52 Mg C ha⁻¹ in orchards and other intensively managed woodland plantations.

Zoom images of many of these findings can also be found in **Appendix Figures S2-S3**.

Map Uncertainty

We mapped the uncertainty in our estimates of aboveground carbon density by combining errors from two important sources (**Figure 3, Appendix Figure S4**). The first is the uncertainty in the relationship between airborne LiDAR-based and field-estimated aboveground carbon density (ACD) (**Figure 25**; see Methods). Our validation process indicated that the mean error of LiDAR-based estimates of ACD is 11.6%. The second source of error is associated with the modeling of the LiDAR canopy height throughout Perú. To determine this error, we set aside 536,874 ha throughout the country that were directly measured with airborne LiDAR, but were not used in building the models for national-scale mapping (see Technical Methodology), and we used these pixels to calculate the root mean squared error (RMSE) between LiDAR-based ACD and RFML-based ACD. These RMSE results were compiled into ten bins across the range of predicted ACD. A polynomial was fit to these data (**Appendix Figure S5**), and was used to determine the uncertainty as a function of mean estimated ACD. These two sources of error were combined as the square root of the sum of the two squared errors, and the geospatial uncertainties were applied to the countrywide map (**Figure 3, Appendix Figure S4**).

In lowland Amazonian forests, our estimated geospatial uncertainty ranges from 5-15% in the highest biomass forests to 20-25% in lower-biomass swamp and floodplain forest (**Figure 3**). These percentage uncertainties equate to absolute errors of up to about 30-40 Mg C ha⁻¹ (**Appendix Figure S4**). In deforested zones of the Amazonian lowlands, geospatial uncertainty increases to about 50-60% of the per-hectare carbon stocks, or about 1-15 Mg C ha⁻¹. Near the Andean treeline, uncertainties increase further to approximately 35-45% on any given hectare, or about 8-25 Mg C ha⁻¹. On the dry leeward side of the Andes, geospatial uncertainty rapidly increases to 60-80%, owing to the fact that we only lightly sampled these types of environments with the LiDAR. Importantly, these large relative uncertainties, when applied to the extremely low aboveground carbon stocks of these dry ecosystems, results in absolute errors of less than 4 Mg C ha⁻¹.

Field-based Map Validation

Validation using 57 one-hectare field plots indicated high precision and accuracy (slope = 1.01; R² = 0.73) of the map of aboveground carbon stocks (**Figure 4**). Our national map over-estimated plot-based carbon stock estimates by approximately 10 Mg C ha⁻¹. Given the inherent uncertainty of 15-30% in field-estimated carbon stocks at one-hectare resolution for forests¹⁸ and shrublands¹⁹, we considered our bias to be acceptable.

Figure 3

Estimated percentage uncertainty in aboveground carbon stocks at one-hectare resolution for the country of Perú.

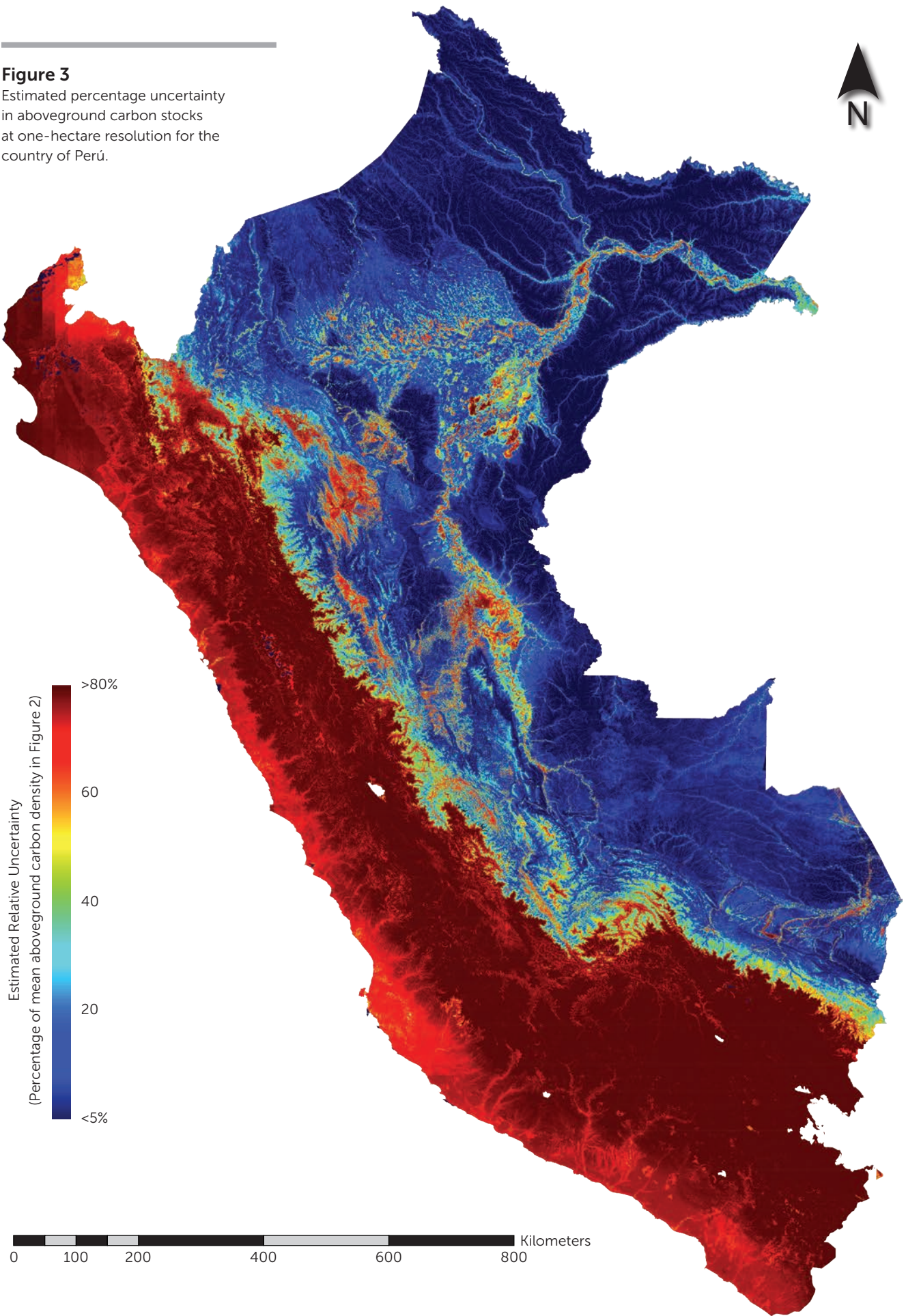
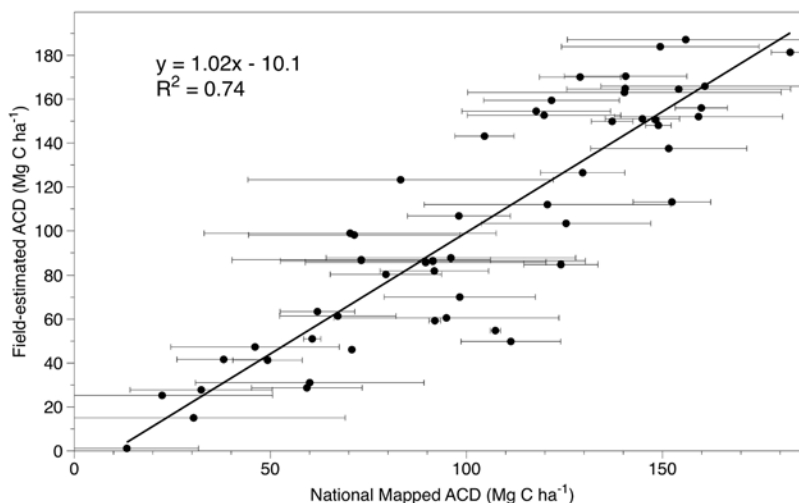


Figure 4

Validation of nationally mapped estimates of aboveground carbon density (ACD) versus field plot inventory estimates of ACD for sites across Northern, Central and Southern Perú.

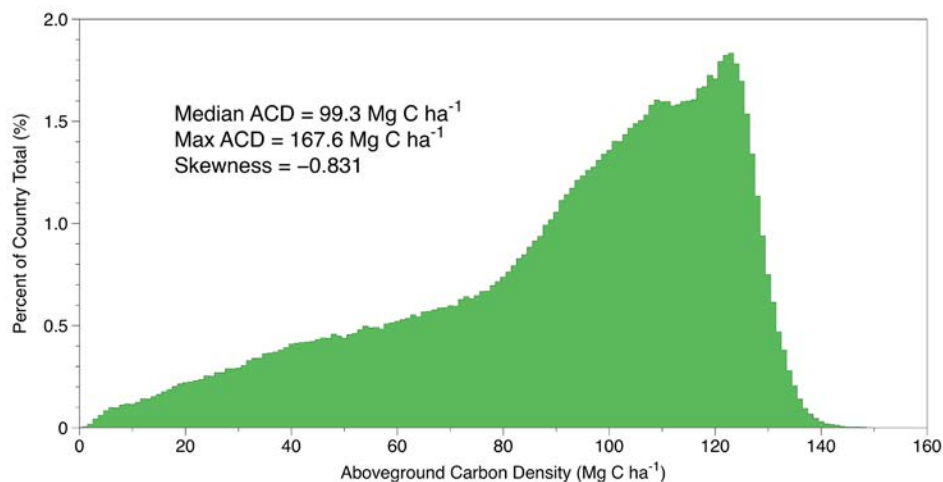


National-scale Variation in Forest Carbon Stocks

Among all Peruvian forests and woodlands nationwide, we found a highly skewed ($\gamma = -0.831$) distribution of aboveground carbon stocks (Figure 5). The median carbon density for all Peruvian forests is $99.3 \text{ Mg C ha}^{-1}$, and the maximum-recorded density is $167.6 \text{ Mg C ha}^{-1}$. More than 50% of all Peruvian forests harbor aboveground carbon densities of more than 100 Mg C ha^{-1} , but only 10% of these exceed 125 Mg C ha^{-1} . The vast majority of these high-biomass forests are located in the lowland and submontane regions of the Amazon, usually below 500 m elevation.

Figure 5

Distribution of aboveground carbon density at one-hectare resolution for forests throughout the country of Perú.



Environmental Controls on Carbon Stocks

Analysis of the environmental variables used in the national mapping methodology revealed that the fractional cover of photosynthetic vegetation (PV) is the most important geographic factor predicting aboveground carbon stocks throughout Perú (Figure 6). Fractional PV is a quantitative metric derived from Landsat satellite imagery, and it is known to be highly sensitive to the percentage cover of woody canopy plants²⁰⁻²². As a result, fractional PV cover

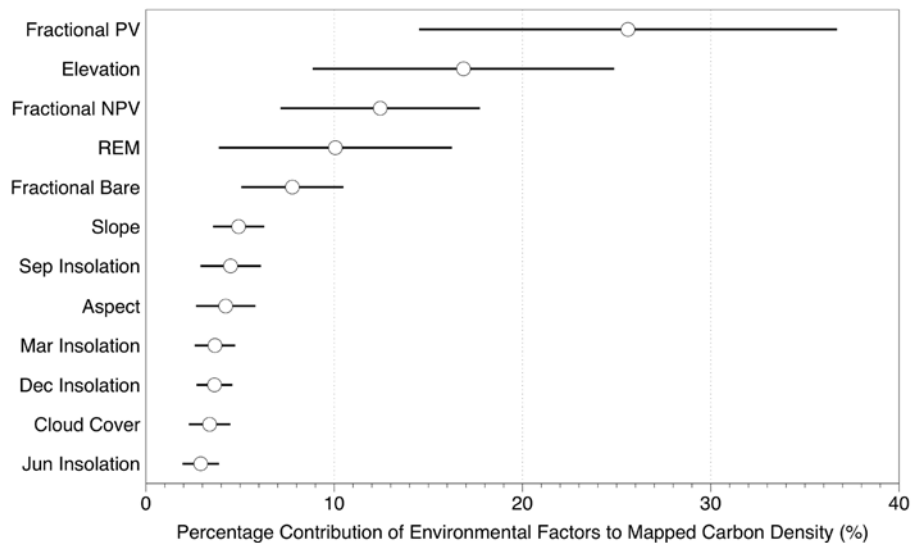


Figure 6

Relative importance of satellite-derived environmental variables in the prediction and mapping of aboveground carbon density (ACD) throughout Perú. Key: (i) Fractional PV is the percent green canopy cover in each hectare; (ii) Elevation is the height of the land in meters above sea level; (iii) Fractional NPV is the percent non-photosynthetic vegetation or dried, exposed vegetation in each hectare — a strong proxy for ecological disturbance; (iv) REM is the relative elevation model depicting local height of the land above nearest water body such as a stream or lake; (v) Fractional Bare is the percent exposed bare surfaces in each hectare — another proxy for ecological disturbance; (vi) Slope is the tilt of the land surface; (vii) Insolation is the average amount of solar energy striking the land surface at four points in the year (Sept, Mar, Dec, June); (viii) Cloud cover is the fraction of the year that each hectare is cover in clouds, thereby reducing energy input for vegetation growth.

is often spatially correlated with aboveground carbon stocks in a wide range of ecosystems, from arid shrublands to humid tropical forests²³⁻³¹. As such, it accounted for 26% ($\pm 9\%$) of the carbon stocks mapped with the airborne LiDAR throughout Perú.

Second to fractional PV cover, changes in elevation also had a large effect ($18\% \pm 6\%$) on mapped carbon stocks (Figure 6). Furthermore, after removing un-forested and/or deforested areas from the analysis, we found that the relationship between elevation and carbon stocks was even clearer (Figure 7). Independent of floristic composition, precipitation, micro-environment, or other factors, average aboveground carbon density decreases by about 2.3% per meter of elevation gain. However, there is enormous variation within each elevation zone, with the maximum variation occurring in the lowlands and sub-montane ecosystems below about 1500 meters a.s.l. Moreover, the lowlands are about equally likely to harbor very low or high carbon densities (Figure 7, less than 400 m a.s.l.). Areas of suppressed carbon storage in the lowlands are due to hydrological conditions such as anoxia (swamp-like conditions) and changes in soil fertility associated with underlying geologic substrate²⁷. In the sub-montane region of 900-1600 m a.s.l., carbon stocks remain highly variable and show high-spots particularly in the 1200-1300

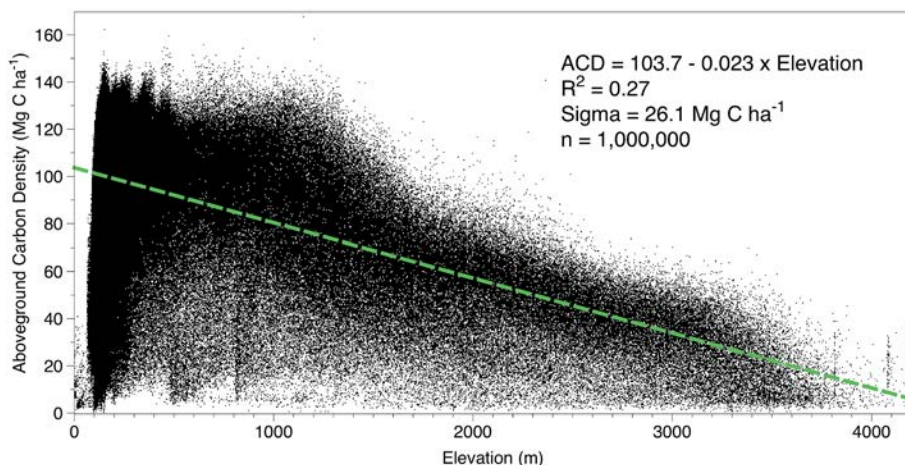


Figure 7

Changes in aboveground carbon density (ACD) with elevation throughout the forested portions of Perú. Each data point represents one hectare.

m elevation zone. At treeline, which varies from about 3700-4200 m a.s.l., depending upon local conditions and past land use, carbon stocks average 11 Mg C ha⁻¹ (Figure 7). Even at these high altitudes, it is possible to find forests with carbon stocks as high as 30 Mg C ha⁻¹.

At the national scale, other critically important determinants of aboveground carbon stocks include the fractional cover of non-photosynthetic vegetation (NPV), relative elevation (REM) above nearest water body, and fractional cover of bare surfaces (Figure 6). Together, these three factors account for about 32% of the variation in aboveground carbon stocks throughout Perú. Fractional NPV and bare substrate cover are well-known metrics of forest disturbance including natural processes such as landslides, blow-downs, and gap dynamics^{32, 33}, as well as human-driven disturbance such as selective logging, fire, and other processes that thin vegetation canopies without complete removal of them^{25,34-39}. REM is a proxy for both water access by plants and water-related disturbance via flooding.

Compared to the top five factors predicting carbon stocks in Perú, the remaining satellite-based variables each accounted for about 3-5% of the total variation throughout the country (Figure 6). These included topographic slope and aspect, solar insolation throughout the year, and cloudiness. However, combined, these factors did account for about 30% of the mapped variation, and thus we consider them all to be important in creating the high-resolution aboveground carbon map for Perú (Figure 2).

Carbon by Regional Government

Aboveground carbon densities and total carbon stocks varied enormously by Peruvian Regional government, which were formerly called Departments (Table 1). Loreto contains 53% of Perú's aboveground carbon stock, owing to the large size of this Region and its particularly high carbon densities (98.8 ± 29.4 Mg C ha⁻¹). The second and third largest Regional stocks are found in Ucayali and Madre de Dios, respectively. Together these two Regions contain 26% of the total Peruvian carbon stock. Other Regions with large stocks include San Martín, Amazonas, Cusco, Junín, Huánuco, Pasco and Puno, although together they comprise just 18.5% of the total aboveground carbon stock of the country.

We present higher-resolution maps of the top ten Regional governments in Figures 8-17. Many of the natural and human-mediated patterns in carbon stocks can be readily viewed in these maps, with additional findings as follows:

1. In lowland Regions such as Loreto, Ucayali and Madre de Dios (Figures 8-10), topographic incisions associated with small river and stream activity harbor carbon stocks that are 30-50% lower than their non-incision or non-riparian counterparts.
2. Large active floodplains associated with the Amazon (Figure 8), Ucayali (Figure 8-9), and Madre de Dios and Las Piedras rivers (Figure 10) contain 50-80% lower carbon stocks than neighboring terra firme forests.
3. Regions containing extensive swaths of submontane Andean ecosystems such as San Martín, Amazonas, Junín and Pasco (Figures 11-12, 14, 16) are prone to high variance in carbon stocks due to a combination of natural and human-mediated factors. These include natural landslides on slopes

exceeding 38 degrees, mesoclimatic effects associated with topographic aspect (local leeward conditions), and extensive deforestation and forest degradation.

4. Decreases in carbon stocks at higher elevations of 2500 to 4000 m a.s.l. are particularly apparent in the Regions of San Martín, Junín, Huánuco, Pasco and Puno (Figures 11, 14-17). The elevational-rate of forest carbon decrease is discussed earlier in the report.

Region	Area (ha)	Mean Carbon Density (Mg C ha ⁻¹)	SD of Carbon Density (Mg C ha ⁻¹)	Total Carbon Stock (Tg C)	Proportion of Perú (%)
Amazonas	3,930,390	61.9	38.7	242.9	3.51
Ancash	3,595,941	2.3	2.6	8.1	0.12
Apurímac	2,111,640	1.0	2.1	2.2	0.03
Arequipa	6,325,762	2.2	2.6	14.2	0.21
Ayacucho	4,349,951	4.7	13.8	20.4	0.29
Cajamarca	3,304,619	9.2	17.0	30.5	0.44
Callao	14,167	6.4	2.8	0.1	0.01
Cusco	7,207,883	32.2	38.8	231.7	3.35
Huancavelica	2,206,335	1.8	4.2	3.9	0.06
Huánuco	3,720,347	35.2	37.5	130.6	1.89
Ica	2,108,125	7.7	4.2	16.1	0.23
Junín	4,399,697	33.4	37.5	146.4	2.11
La Libertad	2,529,588	4.0	8.2	10.0	0.14
Lambayeque	1,434,306	3.1	2.6	4.4	0.06
Lima	3,499,260	3.3	3.0	11.6	0.17
Loreto	37,511,259	98.8	29.4	3685.1	53.24
Madre de Dios	8,504,866	96.4	23.0	819.2	11.83
Moquegua	1,580,513	2.7	3.2	4.3	0.06
Pasco	2,411,598	51.2	42.5	123.3	1.78
Piura	3,605,927	3.3	4.6	11.7	0.17
Puno	6,796,462	15.6	32.3	106.0	1.53
San Martín	5,096,436	59.8	37.8	303.8	4.39
Tacna	1,608,229	2.9	2.6	4.7	0.07
Tumbes	469,182	10.3	7.0	4.3	0.06
Ucayali	10,533,060	93.7	31.1	986.8	14.26

Table 1

Mean and standard deviation of aboveground carbon density, and total aboveground carbon stock, for each Peruvian Region. The proportion of carbon stocks in each Region relative to the total carbon stock of Peru is also given. SD = standard deviation. Tg = Teragram = one million metric tons.



Figure 8

Aboveground carbon density of the Peruvian Region of Loreto.

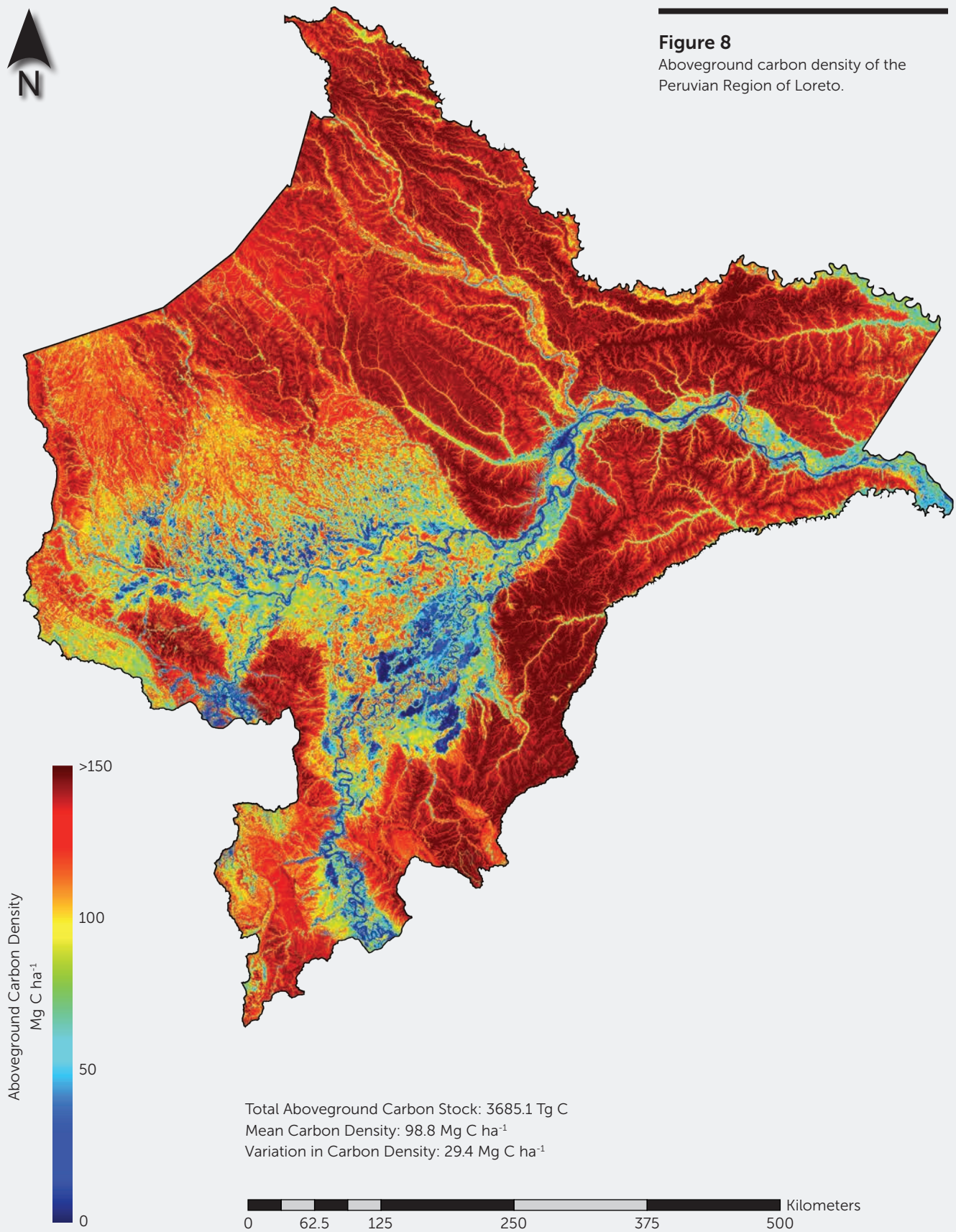
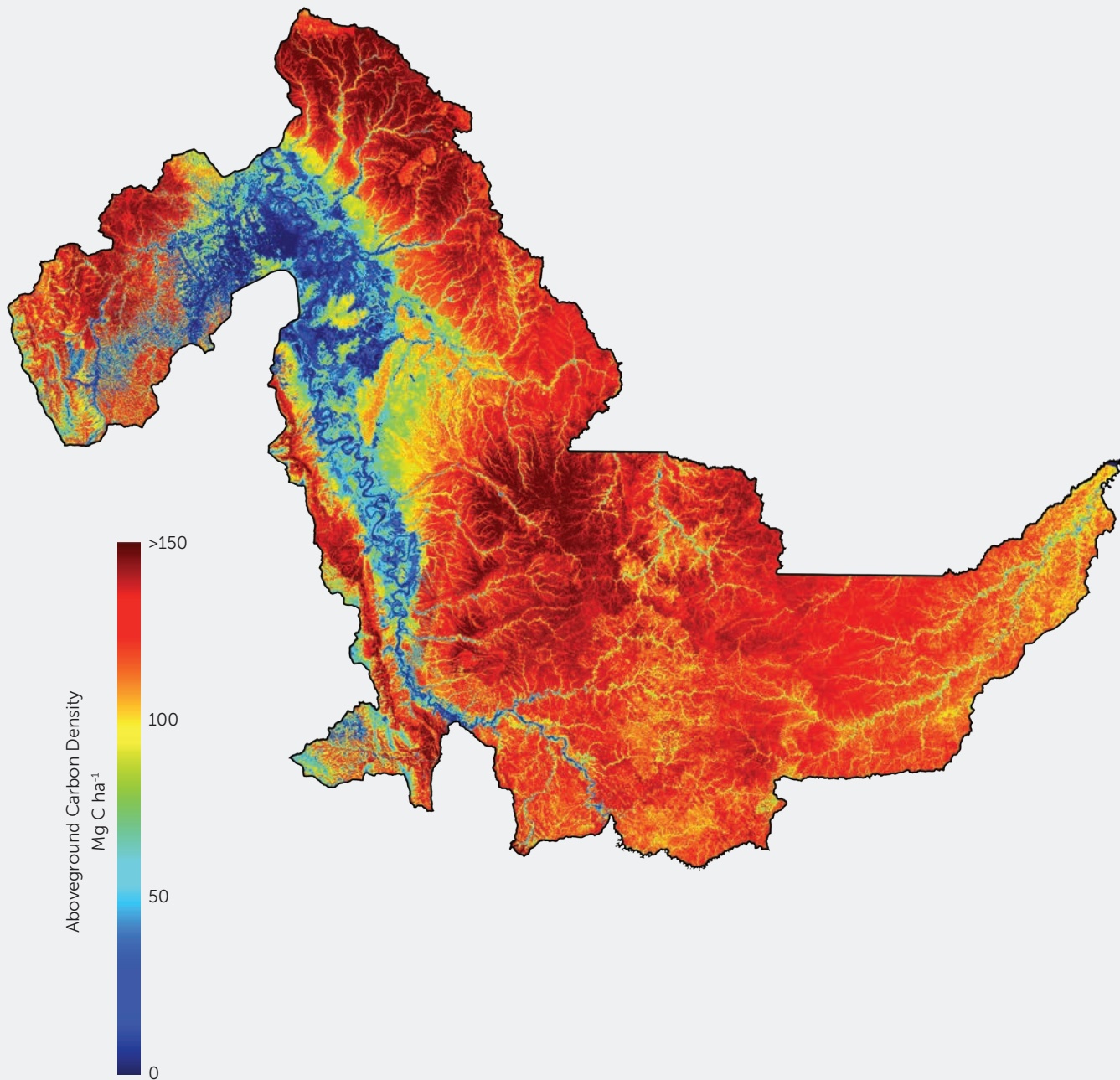


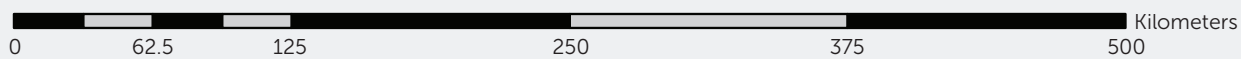


Figure 9

Aboveground carbon density of the Peruvian Region of Ucayali.



Total Aboveground Carbon Stock: 986.8 Tg C
Mean Carbon Density: 93.7 Mg C ha⁻¹
Variation in Carbon Density: 31.1 Mg C ha⁻¹



Madre de Dios



Figure 10

Aboveground carbon density of the Peruvian Region of Madre de Dios.

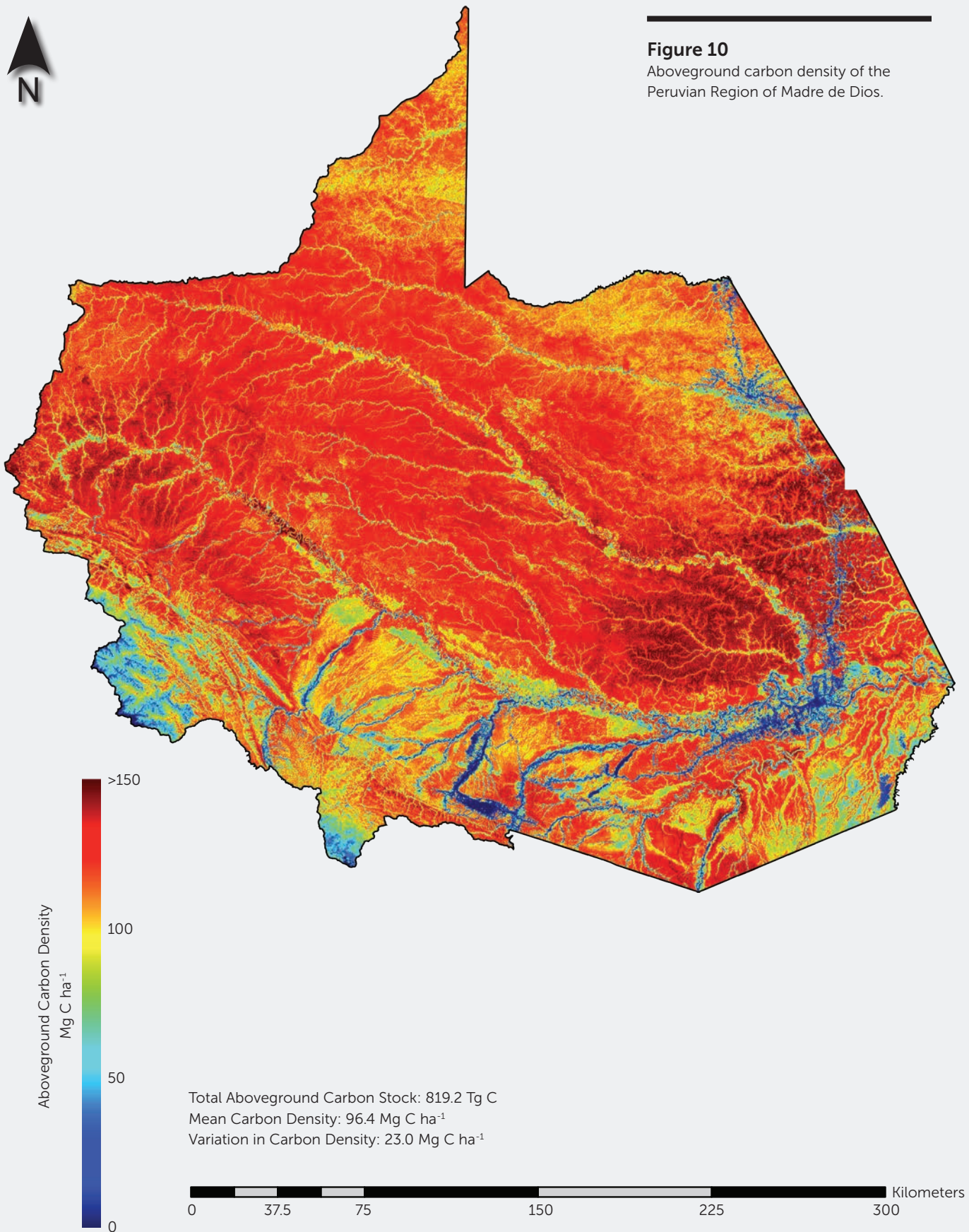
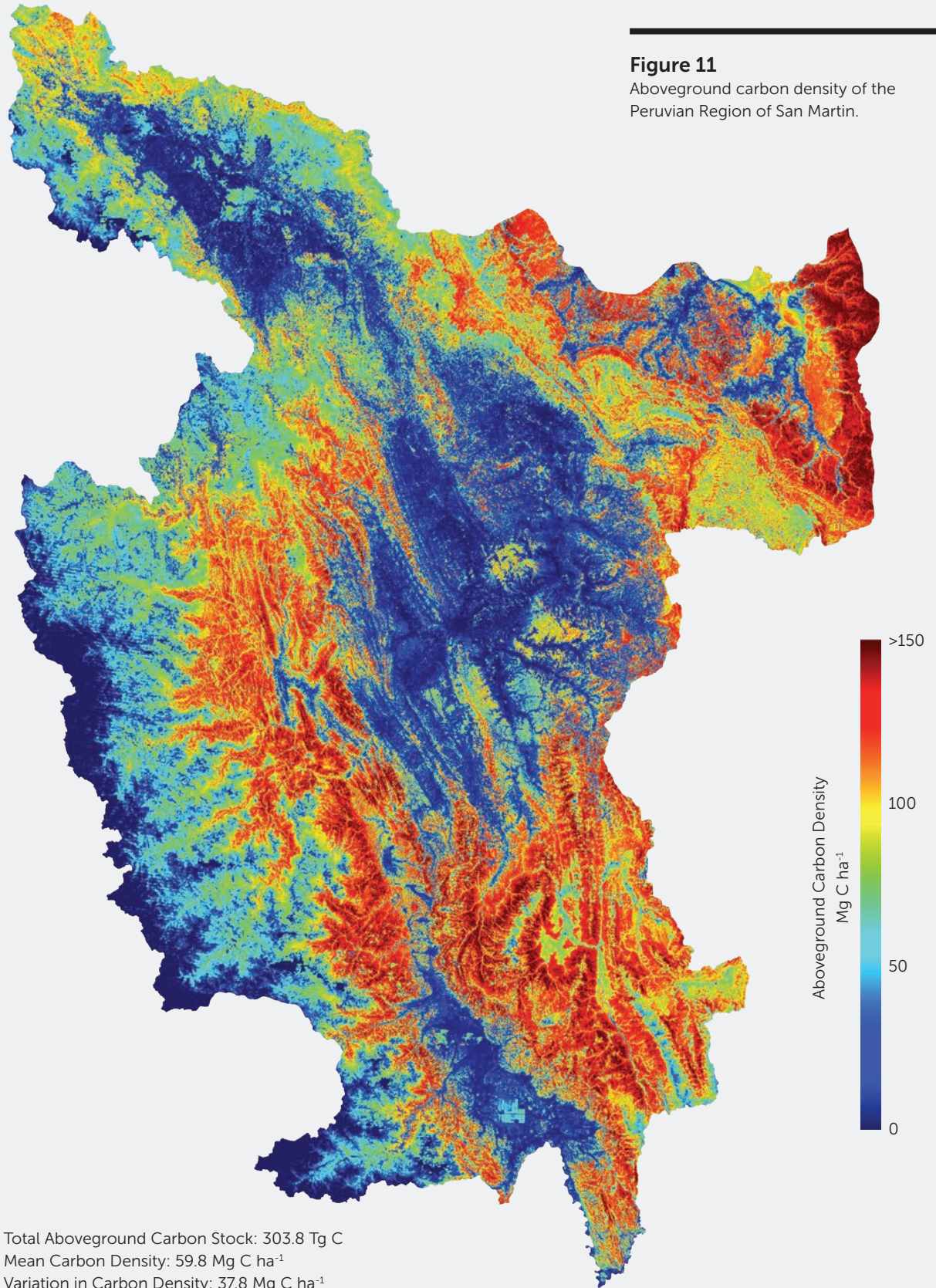




Figure 11

Aboveground carbon density of the Peruvian Region of San Martin.



0 25 50 100 150 200 Kilometers

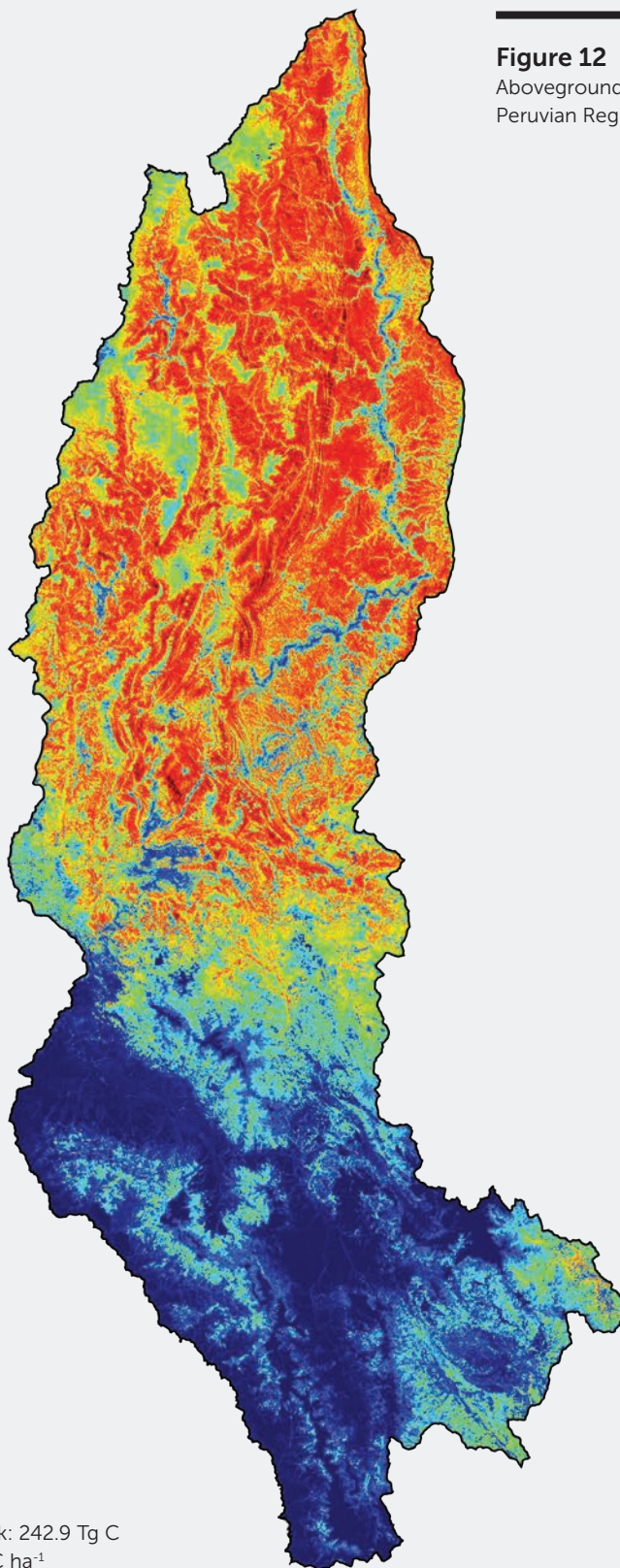


Figure 12

Aboveground carbon density of the Peruvian Region of Amazonas.



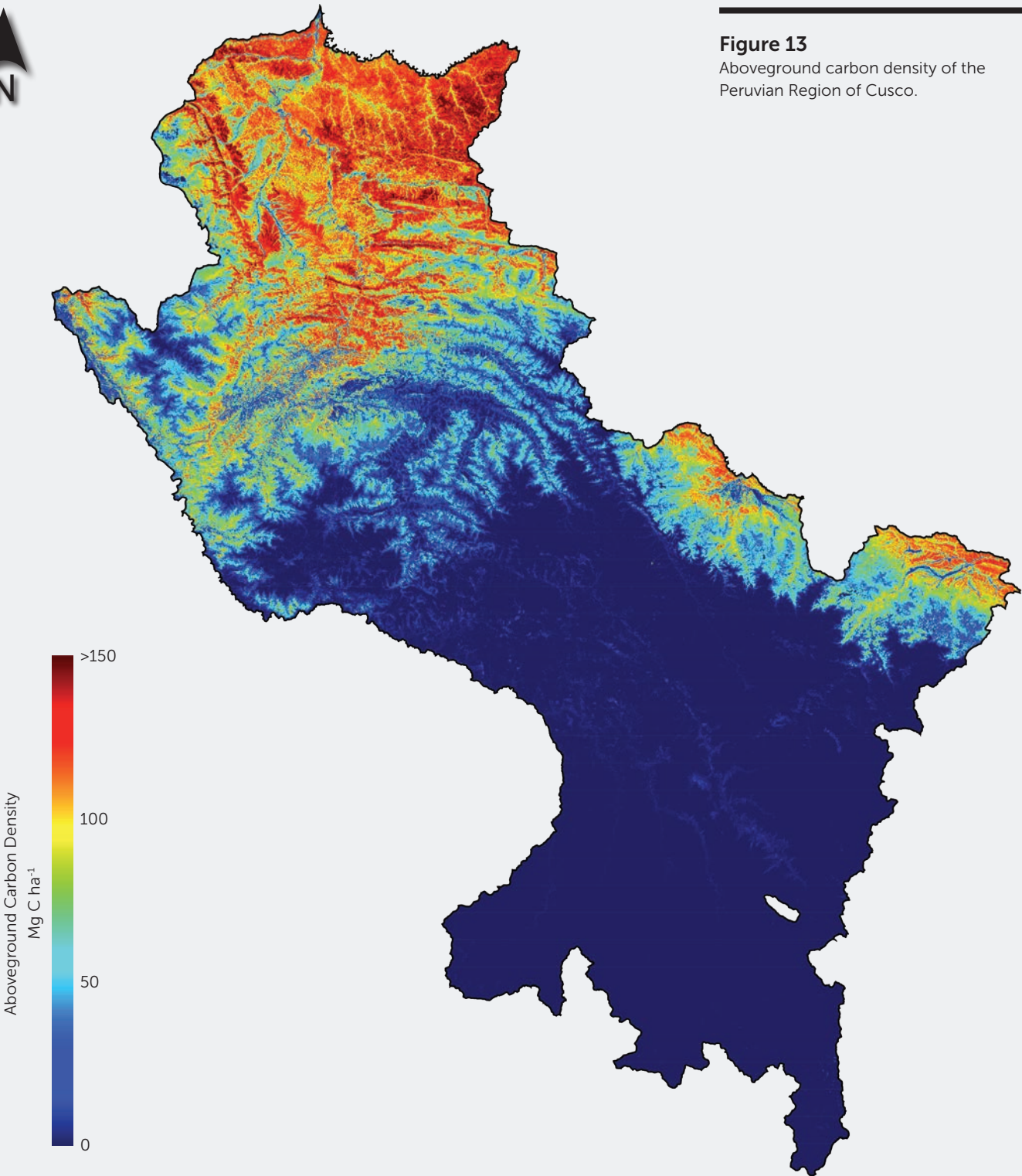
Total Aboveground Carbon Stock: 242.9 Tg C
Mean Carbon Density: 61.9 Mg C ha⁻¹
Variation in Carbon Density: 38.7 Mg C ha⁻¹





Figure 13

Aboveground carbon density of the Peruvian Region of Cusco.



Total Aboveground Carbon Stock: 231.7 Tg C
Mean Carbon Density: 32.2 Mg C ha⁻¹
Variation in Carbon Density: 38.8 Mg C ha⁻¹

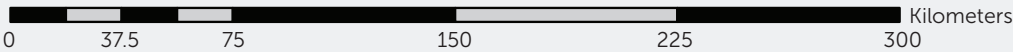
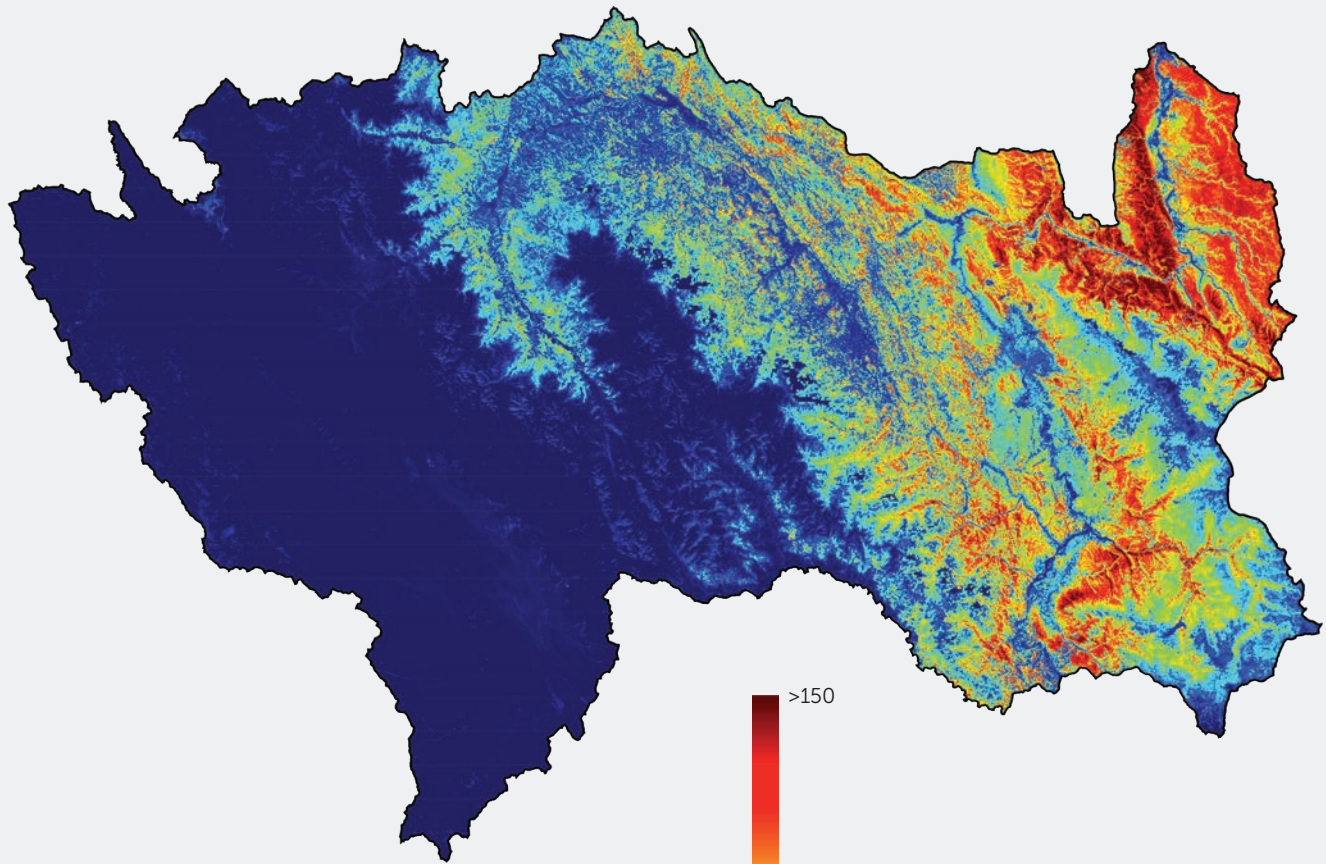




Figure 14

Aboveground carbon density of the Peruvian Region of Junín.



Total Aboveground Carbon Stock: 146.4 Tg C
Mean Carbon Density: 33.4 Mg C ha⁻¹
Variation in Carbon Density: 37.5 Mg C ha⁻¹

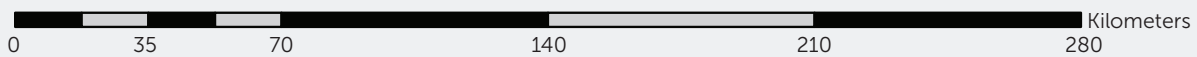
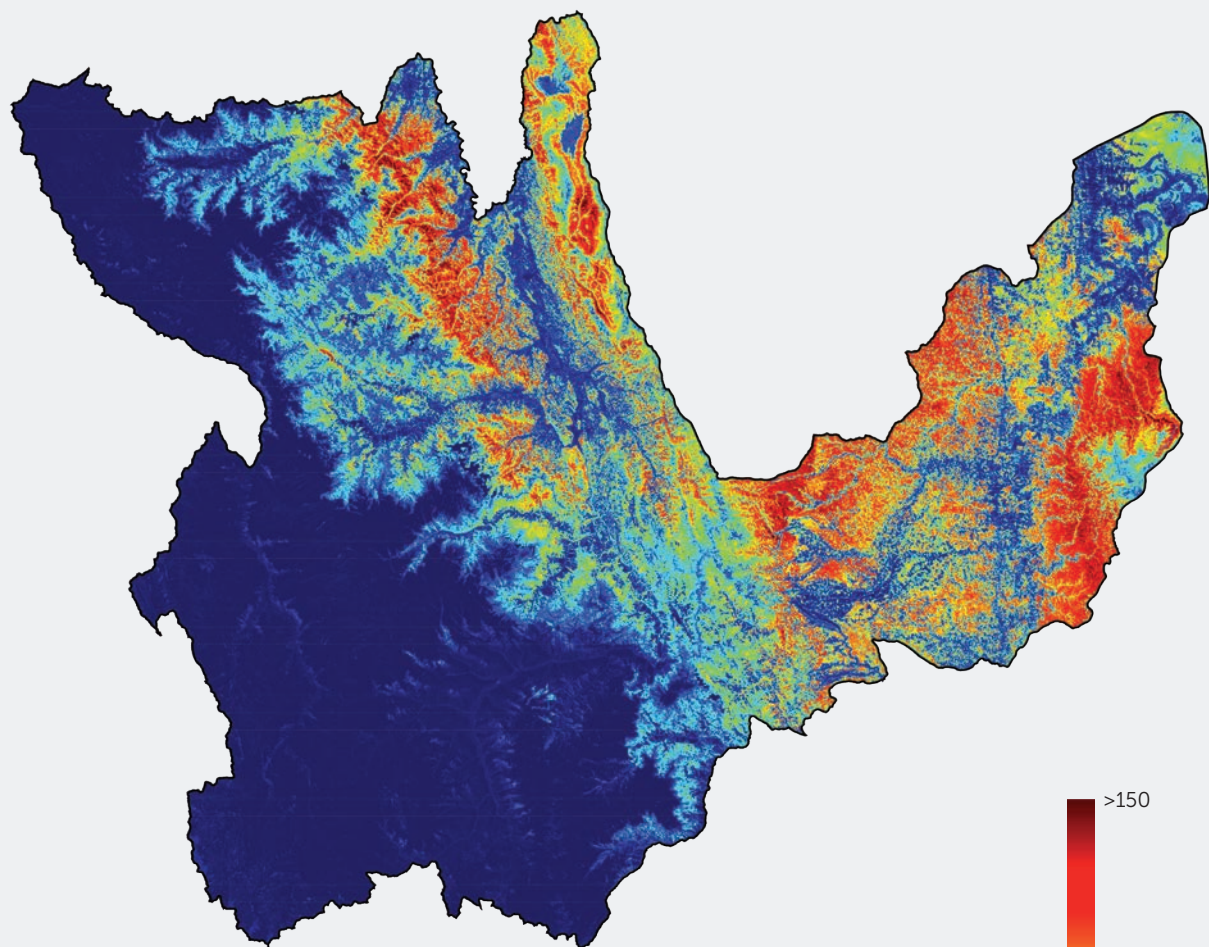




Figure 15

Aboveground carbon density of the Peruvian Region of Huánuco.



Total Aboveground Carbon Stock: 130.6 Tg C
Mean Carbon Density: 35.2 Mg C ha⁻¹
Variation in Carbon Density: 37.5 Mg C ha⁻¹

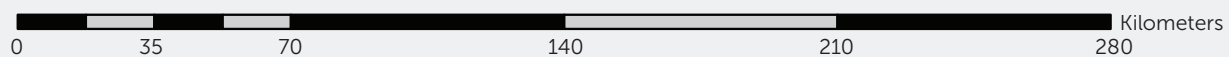
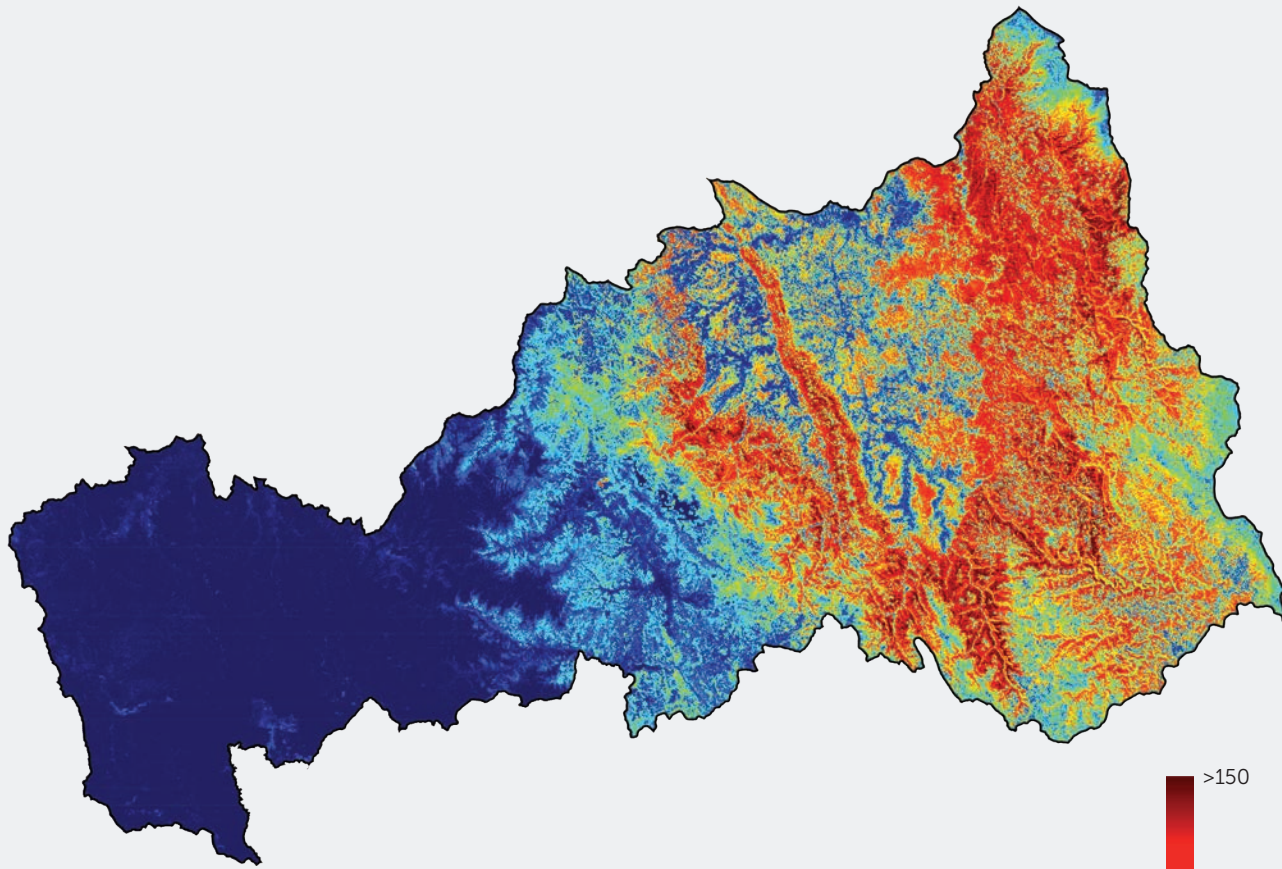




Figure 16

Aboveground carbon density of the Peruvian Region of Pasco.



Total Aboveground Carbon Stock: 123.3 Tg C
Mean Carbon Density: 51.2 Mg C ha⁻¹
Variation in Carbon Density: 42.5 Mg C ha⁻¹

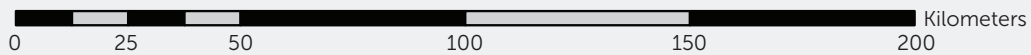
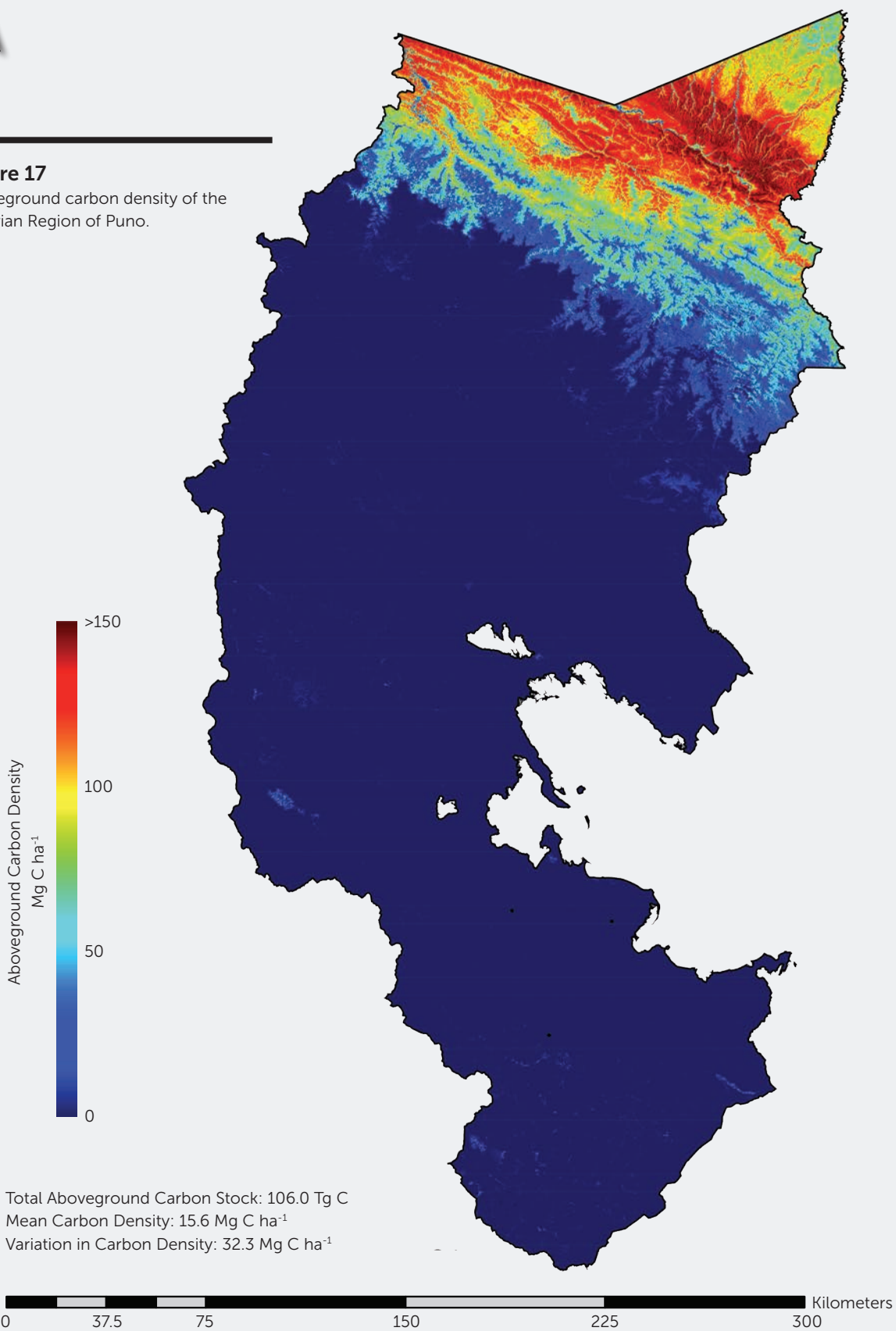




Figure 17

Aboveground carbon density of the Peruvian Region of Puno.



Carbon in Protected Areas

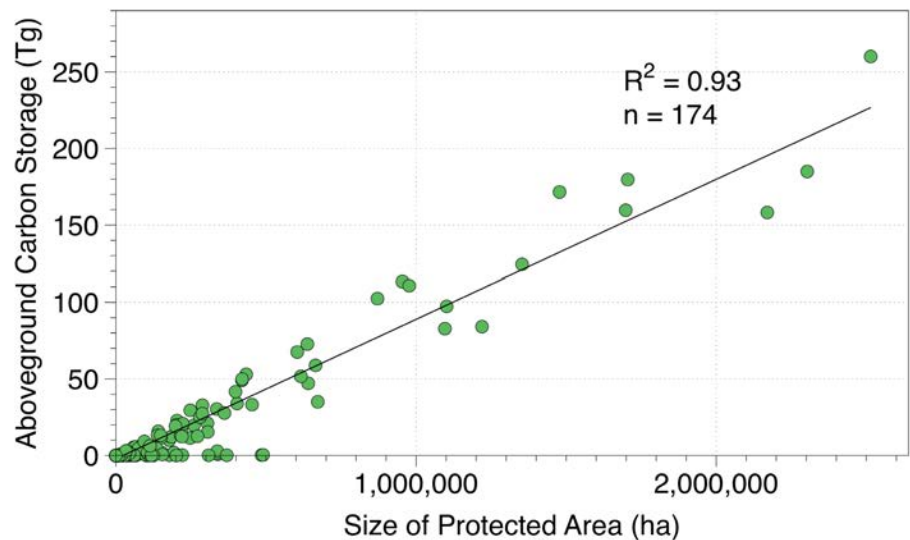
We assessed the aboveground carbon density and total carbon stocks of 174 protected areas within Perú (Table 2, on page 30). A total of 1.816 Pg (billion metric tons) of carbon are stored in vegetation within these protected areas, or about 26% of the total estimated aboveground carbon stocks found within Perú. This leaves up to 74% of aboveground carbon stocks outside of these protected areas.

The largest stocks are found in the ten largest forest reserves, including the Alto Purus, Manu, Cordillera Azul and Bahuaja Sonene national parks, Pacaya Samiria and Pucacuro national reserves, and the Alto Nanay-Pintuyacu Chambira, Ampiyacu Apayacu, Sierra del Divisor, Yaguas and Santiago Comaina reserves. These protected areas alone comprise 85% of the total aboveground carbon stores among the 174 protected areas assessed. Within humid Amazonian and Andean forests, the size of each protected area is highly correlated with its total aboveground carbon stock ($R^2 = 0.93$; Figure 18), with each hectare of protection adding an average 95.1 Mg or metric tons of carbon aboveground to the biosphere, and more to belowground carbon stocks (not estimated here).

In terms of carbon stocks per unit area protected, reserves such as Ampiyacu Apayacu, Alto Nanay-Pintayacu Chambira, and Sierra del Divisor contain the highest carbon densities of 119.2 ± 17.5 Mg C ha⁻¹ (Table 2). Other notable protected areas with high carbon densities include Alto Purus (103.7), Purus (99.0), Santiago Comaina (96.3), Yanesha (94.4), Manu (94.1), Allpahuayo Mishana (93.2), Cordillera Azul (92.0), and Tambopata (89.3). Given the protected area status of these reserves, differences in carbon density are most likely driven by the environmental factors previously discussed, including elevation, canopy structure and natural disturbance regimes, and climate.

Figure 18

Relationship between the size of protected areas in Perú and their total carbon stored above ground.



Name	Type*	Area (ha)	Mean Carbon Density (Mg C ha ⁻¹)	SD of Carbon Density (Mg C ha ⁻¹)	Total Carbon Stock (Tg C)
A.B. del Canal Nuevo Imperial	4	17	13.7	3.6	< 0.001
Abra Málaga	8	1032	18.5	16.5	0.019
Abra Málaga Thastayoc - Royal Cinclodes	8	74	0.8	0.7	< 0.001
Abra Patricia-Alto Nieva	8	1423	57.0	8.3	0.081
Airo Pai	3	247884	119.3	15.2	29.547
Albúfera de Medio Mundo	8	685	6.1	2.4	0.003
Allpahuayo Mishana	2	58084	93.4	25.3	5.424
Alto Mayo	4	177740	57.9	24.1	10.009
Alto Nanay-Pintuyacu Chambira	8	954646	118.7	11.6	113.361
Alto Purus	1	2514790	103.7	11.4	260.091
Amarakaeri	3	403828	84.2	20.1	33.975
Amazon Natural Park	8	64	82.0	25.3	0.005
Amazon Shelter	8	12	38.0	14.6	< 0.001
Ampay	5	3847	4.5	5.6	0.017
Ampiyacu Apayacu	8	434182	122.2	10.6	53.037
Ancón	7	2186	11.3	5.7	< 0.001
Angostura-Faical	8	8868	16.1	2.8	0.143
Ashaninka	3	184462	66.6	27.3	12.271
Bahuaja	8	6	65.2	42.6	< 0.001
Bahuaja Sonene	1	1102040	88.4	25.6	97.372
Berlin	8	61	40.9	9.0	0.002
Boa Wadack Dari	8	23	76.5	14.5	0.002
Bosque Benjamín I	8	28	98.1	17.4	0.003
Bosque Benjamín II	8	29	108.0	14.1	0.003
Bosque Benjamín III	8	24	69.5	18.9	0.002
Bosque de Palmeras de la Comunidad Campe	8	5925	4.1	1.7	0.024
Bosque de Pómac	6	10919	31.7	17.3	0.346
Bosque de Puya Raymondi - Titankayocc	8	6265	0.6	1.0	0.004
Bosque de Zarate	7	546	3.0	1.6	0.002
Bosque Huacrupe-La Calera	8	7327	2.4	0.6	0.017
Bosque Moyan-Palacio	8	8527	2.5	1.2	0.021
Bosque Nublado	8	3372	48.6	14.1	0.164
Bosque Seco Amotape	8	125	4.5	0.4	0.001
Bosques de Neblina y Paramos de Samanga	8	2906	12.0	12.4	0.035

Table 2

Mean and standard deviation of aboveground carbon density, and total aboveground carbon stock, for protected areas in Perú. SD = standard deviation. Tg = Teragram = one million metric tons.

Table 2 (cont.)

Mean and standard deviation of aboveground carbon density, and total aboveground carbon stock, for protected areas in Perú. SD = standard deviation. Tg = Teragram = one million metric tons.

Name	Type*	Area (ha)	Mean Carbon Density (Mg C ha ⁻¹)	SD of Carbon Density (Mg C ha ⁻¹)	Total Carbon Stock (Tg C)
Bosques Nublados de Udimá Sector Centro	8	73	3.4	2.2	< 0.001
Bosques Nublados de Udimá Sector Norte	8	2273	2.4	1.2	0.005
Bosques Nublados de Udimá Sector Sur	8	9889	10.2	7.9	0.100
Bosques Secos Salitral - Huarmaca Sector Sur	8	3703	2.3	1.3	0.009
Bosques Secos Salitral - Huarmaca Sector Norte	8	25319	1.9	0.6	0.049
Calipuy	2	64099	1.8	1.6	0.112
Calipuy	5	4499	1.2	0.9	0.005
Camino Verde Baltimore	8	20	109.9	13.2	0.002
Canoncillo	8	1506	4.6	1.3	0.007
Cerros de Amotape	1	152933	12.6	6.6	1.921
Chacamarca	6	2436	0.4	1.4	0.001
Chancaybaños	7	2659	4.3	2.1	0.012
Chaparrí	8	40524	2.1	1.0	0.086
Chayu Naín	3	23620	57.5	21.1	1.303
Checca	8	563	0.1	0.0	< 0.001
Choquechaca	8	2071	1.8	2.5	0.004
Choquequirao	8	103803	7.7	10.9	0.789
Comunal Tamshiyacu Tahuayo	8	420071	117.0	17.7	49.154
Copallín	8	11566	32.0	16.7	0.370
Cordillera Azul	1	1353380	92.0	21.8	124.463
Cordillera de Colán	5	39232	53.7	21.6	2.105
Cordillera Escalera	8	150568	77.8	21.3	11.709
Cordillera Huayhuash	7	67570	2.9	2.5	0.197
Cutervo	1	8231	28.2	16.8	0.232
De la Pampa de Ayacucho	6	298	1.4	2.9	< 0.001
El Angolo	8	65979	2.2	1.9	0.144
El Gato	8	44	76.3	16.3	0.003
El Sira	3	616380	83.9	29.0	51.700
Gotas de Agua I	8	3	2.3	0.3	< 0.001
Gotas de Agua II	8	9	2.4	0.5	< 0.001
Güepí-Sekime	1	203676	112.4	15.1	22.875
Habana Rural Inn	8	29	56.0	15.1	0.002
Hatun Queuña - Quishuarani Ccollana	8	232	0.6	0.5	< 0.001
Herman Dantas	8	49	112.6	17.9	0.006
Hierba Buena - Allpayacu	8	2282	34.9	14.2	0.080

Name	Type*	Area (ha)	Mean Carbon Density (Mg C ha ⁻¹)	SD of Carbon Density (Mg C ha ⁻¹)	Total Carbon Stock (Tg C)
Huamanmarca-Ochuro-Tumpullo	8	15680	0.3	0.4	0.005
Huascarán	1	339991	2.7	3.4	0.848
Huaylla Belén - Colcamar	8	6341	20.5	18.9	0.130
Huayllapa	8	21043	2.9	2.3	0.060
Huayllay	5	6737	0.4	0.4	0.003
Huaytapallana	8	22384	3.0	4.5	0.067
Huimeki	3	141258	112.5	16.5	15.888
Huiquilla	8	1139	23.1	15.7	0.026
Humedales de Puerto Viejo	7	276	5.8	2.2	0.002
Humedales de Ventanilla	8	283	7.5	3.4	0.002
Ichigkat Muja-Cordillera del Cóndor	1	88506	81.5	16.4	7.111
Illescas	7	37886	0.4	0.2	0.016
Imiria	8	135655	33.9	24.5	4.603
Inotawa-1	8	57	104.4	25.7	0.006
Inotawa-2	8	16	106.9	23.4	0.002
Japu - Bosque Ukumari Llaqta	8	18762	34.8	23.9	0.645
Jirishanca	8	12085	2.4	2.2	0.029
Junín	2	52561	5.2	7.2	0.134
Juningue	8	37	38.4	16.7	0.001
La Huerta del Chaparri	8	50	1.3	0.8	< 0.001
La Pampa del Burro	8	2781	53.8	11.0	0.150
Lachay	2	5131	7.0	2.2	0.036
Laguna de Huacachina	7	2457	10.3	1.0	0.025
Lagunas de Mejía	5	726	10.2	5.2	0.007
Laquipampa	8	8371	2.0	1.5	0.017
Larga Vista I	8	20	58.2	15.2	0.001
Larga Vista II	8	25	52.4	19.7	0.001
Las Panguanas 2	8	1	122.5	0.0	< 0.001
Las Panguanas 3	8	7	118.2	4.1	0.001
Las Panguanas 4	8	5	119.2	4.0	0.001
Llamac	8	6707	2.1	2.1	0.014
Lomas de Ancon	7	10959	4.8	1.6	0.052
Lomas de Atiquipa	8	19046	5.6	2.5	0.107
Los Chilchos	8	45987	46.6	18.0	2.141
Los Pantanos de Villa	8	256	9.2	3.7	0.002
Machiguenga	3	218926	80.3	26.6	17.549
Machupicchu	6	37300	10.7	13.0	0.396
Manglares de Tumbes	5	3004	14.1	4.3	0.041

Table 2 (cont.)

Mean and standard deviation of aboveground carbon density, and total aboveground carbon stock, for protected areas in Perú. SD = standard deviation. Tg = Teragram = one million metric tons.

Name	Type*	Area (ha)	Mean Carbon Density (Mg C ha ⁻¹)	SD of Carbon Density (Mg C ha ⁻¹)	Total Carbon Stock (Tg C)
Mantanay	8	361	2.5	3.4	0.001
Manu	1	1698530	94.1	26.1	159.718
Matsés	2	420596	118.8	19.2	49.978
Megantoni	5	215854	60.8	27.7	13.116
Microcuenca de Paria	8	767	3.2	2.4	0.002
Milpuj - La Heredad	8	16	2.1	0.6	< 0.001
Nor Yauyos-Cochas	8	221252	1.4	2.2	0.302
Nuevo Amanecer	8	30	116.8	20.8	0.004
Otishi	1	305979	50.8	22.9	15.391
Pacaya Samiria	2	2170220	72.9	29.2	158.286
Pacllon	8	14793	2.2	2.0	0.033
Pagaibamba	4	2038	11.5	7.1	0.023
Pampa Galeras Barbara D' Achille	2	8008	0.2	0.1	0.002
Pampa Hermosa	5	11541	40.7	19.0	0.469
Pampacorral	8	764	0.4	1.0	< 0.001
Panguana	8	132	82.9	21.2	0.011
Paracas	2	335432	12.5	3.5	1.389
Paraíso Natural Iwirati	8	101	93.7	13.7	0.009
Pillco Grande- Bosque de Pumataki	8	275	6.8	7.6	0.002
Pta Salinas, Isla Huampanú, Isla Mazorca	2	13686	2.6	1.1	< 0.001
Pucacuro	2	637916	114.1	11.2	72.758
Pucunucho	8	22	25.2	9.2	0.001
Pui Pui	4	54509	9.6	16.1	0.508
Punta Atico	2	3451	12.2	6.3	0.001
Punta Coles	2	3389	10.3	5.9	0.002
Punta Colorado	2	2190	6.4	0.4	< 0.001
Punta Culebras	2	2932	4.7	1.3	< 0.001
Punta Hornillos	2	2772	13.0	4.8	0.001
Punta La Chira	2	2448	8.5	3.1	< 0.001
Punta La Litera	2	2043	8.8	0.8	0.001
Punta Lomas	2	2398	16.3	2.3	< 0.001
Puquio Santa Rosa	4	68	8.1	3.0	0.001
Purus	3	202659	99.0	11.1	20.050
Qosqocahuarina	8	1824	0.5	0.9	0.001
Refugio K'erenda Homet	8	35	51.5	15.6	0.002
Reserva Paisajistica Cerro Khapia	7	18487	0.3	0.2	0.005
Río Abiseo	1	272428	46.7	33.5	12.640
Río Nieva	7	36344	62.8	15.7	2.281
Sagrada Familia	8	126	67.6	20.3	0.009

Name	Type*	Area (ha)	Mean Carbon Density (Mg C ha ⁻¹)	SD of Carbon Density (Mg C ha ⁻¹)	Total Carbon Stock (Tg C)
Salinas y Aguada Blanca	2	369768	0.6	1.3	0.209
San Antonio	8	352	2.6	5.7	0.001
San Fernando	2	154718	6.4	2.6	0.713
San Juan Bautista	8	25	52.5	33.4	0.001
San Marcos	8	991	13.5	15.2	0.013
San Matias San Carlos	4	149321	88.3	27.9	13.180
Santiago Comaina	7	398488	104.8	15.4	41.720
Sele Tecse-Lares Ayllu	8	974	0.4	0.4	< 0.001
Selva Botanica	8	171	115.1	22.4	0.020
Selva Virgen	8	25	80.4	19.1	0.002
Sierra del Divisor	7	1478180	116.2	15.5	171.671
Sub Cuenca del Cotahuasi	8	490550	0.9	1.5	0.450
Sunchubamba	8	61097	2.4	2.8	0.145
Tabaconas Namballe	5	32267	26.0	20.3	0.837
Tambo Ilusion	8	14	27.1	22.9	< 0.001
Tambopata	2	280234	89.4	20.2	25.046
Taypipiña	8	659	0.1	0.0	< 0.001
Tilacancha	8	6804	3.8	7.0	0.026
Tingo María	1	4776	75.0	20.6	0.358
Titicaca	2	36192	0.8	1.7	0.001
Tumbes	2	19422	20.7	5.2	0.402
Tuntanain	3	94994	97.5	16.3	9.261
Tutusima	8	5	35.3	8.2	< 0.001
Uchumiri	8	10250	0.3	0.4	0.003
Vilacota Maure	8	125175	0.9	1.8	0.110
Yaguas	7	871383	117.6	14.8	102.448
Yanachaga-Chemillén	1	113611	57.5	27.0	6.359
Yanesha	3	33398	92.3	27.4	3.081

*Protected area type:

1. National Park
2. National Reserve
3. Communal Reserve
4. Protected Forest
5. National Sanctuary
6. Historical Sanctuary
7. Reserve Zone
8. Other

Using a strategic and cost-effective combination of airborne LiDAR sampling, tactically placed field calibration plots, freely available satellite data, and a new geostatistical modeling approach, we have shown that a high-resolution geography of aboveground carbon stocks can be derived for a large and environmentally complex country such as Perú. This new carbon geography also includes spatially explicit maps of uncertainty, which is essential in decision-making for conservation, management and policy development efforts associated with ecosystems and societal use of lands. Our effort focused on the mean and uncertainty of aboveground carbon stocks in every hectare of Perú, thereby providing a new basis for all stakeholders, large and small, to participate in improving the use and conservation of ecosystems. Our detailed validation work at multiple steps within the process demonstrates that aboveground carbon stocks can be estimated and mapped with a degree of uncertainty that is indistinguishable from laborious hand-measured, field-based estimates. Moreover, the approach presented here is spatially continuous, and is thus far less prone to uncertainty caused by environmental and human-driven variation in carbon stocks.

Our approach is now established for the country of Perú. Updates to the carbon map, as well as spatially explicit changes in carbon stocks, will be far easier to implement going forward. First, carbon emissions from deforestation, forest degradation and other losses from non-forested ecosystems can be monitored against this high-resolution carbon map over time. This can be done at low cost using free Landsat imagery and with operational forest cover monitoring software such as CLASlite^{22, 40}. Second, any new field plot inventory data can be ingested into the LiDAR-to-carbon stock calibration to improve it over time for all types of ecosystems. This can be done on an opportunistic basis, such as when new ecosystems are considered for more detailed calibration, or as new forest programs are implemented in the future. Finally, the LiDAR component can be updated with cost-effective airborne sampling missions, and likely with far smaller data volume than we used in our effort to geostatistically over-sample the country of Perú. An estimate of the geographic coverage of future airborne LiDAR data needed to update the map is between 300,000 and 500,000 hectares, which can be accomplished in just a few weeks of flight operations with standard LiDAR equipment and processing software. Critically, any loss or gain of uncertainty in the carbon map can be monitored with incoming LiDAR data, allowing for a fine-tuning of the amount of LiDAR sampling required to minimize errors to their low current levels reported here.

Study Region

The study covers the country of Perú. The vast majority of the aboveground carbon is found in humid forests stretching from the Andean treeline to the lowland Amazonian forests as far as the Ecuadorian, Colombian, Brazilian and Bolivian borders. A much smaller amount of dry tropical forest is said to exist primarily in the northern portion of the country, and those areas were fully incorporated in the study. The study also includes less understood regions including Andean tundra (Páramos) and high-altitude grasslands, as well as woodlands and shrublands in the inter-Andean corridor.

General Approach

Our general mapping approach is based on the original high-resolution method presented by Asner⁴¹, with a series of improvements developed through testing and analysis in a wide variety of countries and ecosystems^{27,29-31,42}. The approach combines readily available satellite and geographic information system (GIS) datasets at one-hectare or finer resolution, with airborne LiDAR and field plot calibration data, in a modeling framework to develop maps of aboveground carbon density (ACD; units of Mg C ha⁻¹ = metric tons C ha⁻¹) with spatially-explicit uncertainty estimates (Figure 1).

The core technology is airborne LiDAR, which yields highly detailed measurements of forest canopy height and vertical canopy profile (Box 1) that predictably scale with variation in aboveground carbon stocks. Recent studies of a wide range of vegetation types worldwide demonstrate that airborne LiDAR can be used to estimate ACD at one-hectare resolution with a precision and accuracy matching estimates based on field measurements alone⁴³. When properly calibrated, airborne LiDAR-based and field plot-based estimates of forest carbon stocks approach just 10% absolute disagreement at one-hectare spatial resolution, across a wide range of vegetation types including tropical forests^{44, 45}. This offset of around 10% is lower than the typical errors incurred in field plot-based estimates of tropical forest carbon stocks at one-hectare resolution⁴⁶. This suggests that airborne LiDAR can be used to extend field-plot networks to far larger spatial scales. Critically, airborne LiDAR-estimated stocks of aboveground carbon can be generated over hundreds of thousands of hectares per day — a task that cannot be accomplished with field plots.

A second key aspect of the approach to derive high-resolution carbon maps relies on machine learning algorithms to scale airborne LiDAR samples up to full regional

Figure B1

Example of airborne LiDAR data collected over lowland Amazonia by the Carnegie Airborne Observatory. Laser pulses are sent and returned to a LiDAR sensor on board an aircraft, scanning from side to side as the plane moves forward in the air, creating a 2-D spatial coverage. Each near-infrared wavelength laser beam penetrates the canopy, returning light along its pathway to the ground. This interaction is digitized by the LiDAR receiver, and is used to map vegetation height (top image), underlying terrain (bottom image), and the layering of the vegetation in between (not shown but see Figure B2).

Figure B2

Cross-sectional view of vegetation structure collected by the Carnegie Airborne Observatory LiDAR. Different aspects of the three-dimensional vegetation structure are measured with LiDAR: (A) canopy height, (B) vertical layering or profile, and (C) underlying topography.

What is LiDAR?

Light Detection and Ranging (LiDAR) instruments emit short-duration laser pulses that illuminate a target and measure its location in three dimensions (x, y and z). Because the time elapsed from when the laser pulse is emitted to when it is received is known, as well as the exact position of the sensor in the aircraft (including the roll, pitch, and yaw), the distance to the object can be calculated and the vertical distribution of the surface measured (Figure B1). Airborne LiDAR sensors emit near-infrared laser light, typically between 900 and 1100 nanometers. In this wavelength range, vegetation foliage is partly transmissive,

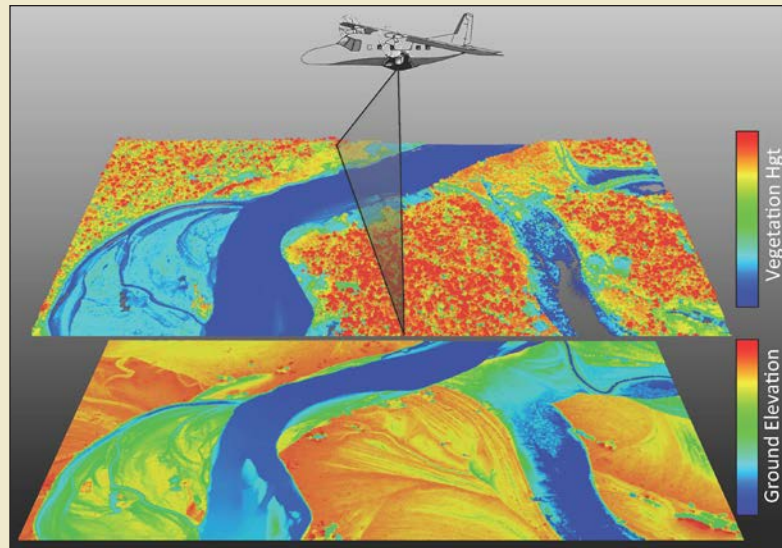


Figure B1

allowing the laser light to pass through the canopy to the ground (Figure B2). With each interaction of this laser light with the canopy elements, such as foliage, some of the light is returned to the sensor, allowing for measurement of the vertical distribution of the canopy tissues. The resolution at which the

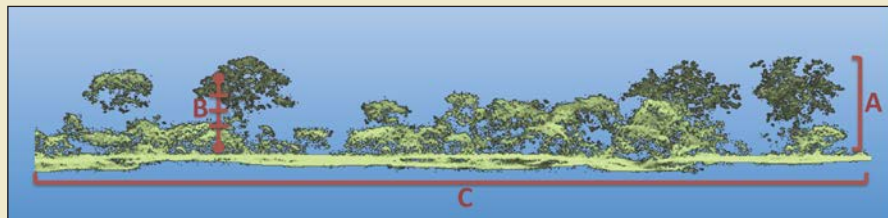


Figure B2

returned laser information is collected depends upon the distance between the sensor and the target. The closer the sensor is to the object, the greater the density of measurements, and the higher the resolution of the LiDAR results. However, the closer the distance, the smaller the area covered by the laser footprint. Although aspects of LiDAR data collection and analysis are expensive, it becomes highly cost-effective over large areas as compared to field surveys, and it is becoming increasingly available in many regions. Furthermore, because of certain fixed costs, the cost of LiDAR per hectare decreases with the area covered during a survey campaign.

or country-wide coverage maps. For decades, stratification and sampling of forests based on *a priori* environmental information, such as elevation or forest type, has served as the method to extrapolate carbon stock estimates from field inventory plots⁴⁷. However, stratification-based methods can yield artificial boundaries in the resulting carbon maps, particularly when applied across highly diverse environmental conditions²⁷. In response to this problem, Baccini et al.² employed a Random Forest Machine Learning (RFML) algorithm to model the relationship between LiDAR-based forest carbon samples and a portfolio of spatially extensive satellite data sets. RFML fits multiple environmental datasets (predictors) to estimates of vegetation structure or biomass (response), as described later. In doing so, a direct scaling of LiDAR samples to full-coverage maps can be derived without artificial boundaries between ecosystems that often occur using traditional stratification approaches. Recently, Mascaro et al.⁴⁸ showed that scaling LiDAR-based carbon samples up to a regional level was 60% more accurate with RFML compared to traditional stratification approaches. In addition, Baccini and Asner⁴⁹ demonstrated that RFML methods can be quickly and cost-effectively updated with new carbon data over time, allowing for dynamic long-term monitoring. Another attractive characteristic of RFML is its ability to provide quantitative information on the environmental variables most predictive of current carbon distributions^{42, 48}.

LiDAR Flight Planning

We used airborne LiDAR to massively sample plant canopy structure throughout the portions of Perú containing woody vegetation. The final map of aboveground carbon density (ACD) relied on an airborne LiDAR sampling approach that supplies data to the RFML upscaling methodology (described below). This required a focus of many aircraft flights on forested ecosystems, but it also included extensive portions of grassland, shrubland, savanna, and open woodland ecosystems. We approached this challenge by over-sampling the land surface using a preliminary stratification of the country as a flight-planning guide. The stratification was based on geologic substrate, soils, topography and large known shifts in community composition. We created this flight-planning map by fusing a variety of previously published and new spatial data sources described here.

We started with a base map called the Geological Map of Perú, provided at 1:1,000,000 scale by INGEMMET⁵⁰. In the time since the publication of this map, field and mapping studies of geology, soil and vegetation patterns in western Amazonia have advanced, and these new data both support and inform the INGEMMET map. These data include a new estimate of lowland geomorphic surfaces derived from extensive Landsat satellite and field sampling of plants and soils. We also used maps of topography from the NASA Shuttle Radar Topography Mission (SRTM), ecological systems from NatureServe.org, and other spatial datasets to extend and enhance detail to the INGEMMET map. We also incorporated information from more recent field inventories of plants and soils for portions of Perú. Integration of these datasets was carried out in ten summary steps:

1. A geological study of the Nanay river drainage indicated that it is distinct from the surrounding, cation-rich Pebas geologic formation, and is more appropriately grouped with the cation-poor Nauta formation⁵¹. This

reassignment was supported by image interpretation and detailed field sampling⁵².

2. Northern Peruvian river terraces dating to the Pleistocene are former courses of large rivers such as the Amazon or Napo, which have been abandoned and now lie above the contemporary floodplain. Due to the high-energy and clay-removing conditions under which these sediments were deposited, they are typically sandy and nutrient-poor. Unlike contemporary floodplain deposits, terraces do not receive regular nutrient inputs from river flooding, resulting in distinct forests adapted to the nutrient poor soils. The INGEMMET map was revised to show the location and extent of these Pleistocene terraces that were delineated using Landsat and SRTM data⁵³.
3. The INGEMMET map designates the land to the east of the Pastaza River and within the Corrientes River drainage as Pebas formation, with the exception of an area between the upper Corrientes and Pastaza Rivers. Based on field sampling of both soils and plants in these drainages⁵², we reassigned this area to the Nauta formation, and expanded the Nauta formation to the west of the Pastaza River.
4. The Pastaza Fan is the second-largest alluvial fan in the world⁵⁴, consisting of volcanoclastic debris transported by the Pastaza River from the Cotopaxi volcano of Ecuador and deposited on the southern extent of the Iquitos uplift. In its southern reaches, between the Pastaza and Marañon Rivers, the Pastaza Fan is permanently inundated due to ongoing subsidence, and this inundation creates massive tracts of forested wetlands. North of the Pastaza River, however, the Pastaza Fan is well drained, and its rich, black soils exert a unique influence on plant species composition. Because of this large difference in hydrologic regimes, and its importance for forest composition and structure, we separated the Upper Pastaza Fan into a new class. In addition, on the basis of Landsat and SRTM data⁵³, we reclassified a portion of the lower Corrientes drainage as Upper Pastaza Fan. Last, because a NatureServe ecological map captures Quaternary features such as the islands of swamp forests in the Upper Pastaza Fan, we inserted these features in the INGEMMET map.
5. In the INGEMMET map, the area to the west of the Madre de Dios River and north of the Manu River is classified as Pleistocene deposition, similar to the recent alluvial deposits south of the Manu River. However, recent geological studies of this region indicate that this area is substantially older and divided into two formations: (a) Miocene age deposits, analogous to the Pebas Formation in northern Perú, and (b) Pliocene age deposits, analogous to the Nauta Formation⁵⁵. The existence of this boundary is further supported by data on soils⁵⁶ and biomass²⁷. We used a combination of Landsat and SRTM data to delineate this boundary.
6. We removed eight areas of Pleistocene deposits from the region west of the Piedras, and merged them with the surrounding Miocene formation. This area is clearly indicated as similar by Espurt et al.⁵⁵, and this homogeneity is readily observed in SRTM elevation data.
7. We used the NatureServe ecological map to add Quaternary fluvial features in the Amazonian lowlands.

8. We incorporated bamboo-dominated forest types using a map provided by Carvalho et al.⁵².
9. We added elevation in 250 meter bands taken from the 90-meter resolution SRTM to the entire country, but these were particularly important in the mountainous regions.
10. To distinguish between intact forest and deforested or degraded areas, we incorporated a map of the fractional cover of photosynthetic vegetation set to a minimum canopy cover of 80% at 30-meter spatial resolution, derived from the CLASlite mapping of Perú^{22, 57}.

Our final flight-planning map is referred to as the GeoEcoElevation map (Figure 19), which partitioned the country into 2375 strata, each of which hypothetically could have a different vegetation carbon density “regime”. Because there are so many strata, we show the GeoEcoElevation map in two parts in Figure 19: (A) the portion delineating the region by the matrix of geology, soils and major floristic communities; and (B) elevation. Knowing that this is likely a case of extreme over-stratification, at least in terms of geographic variation in carbon stocks, we used this stratification to plan flights to ensure maximum sampling density with airborne LiDAR in as many unique regions as could be determined.

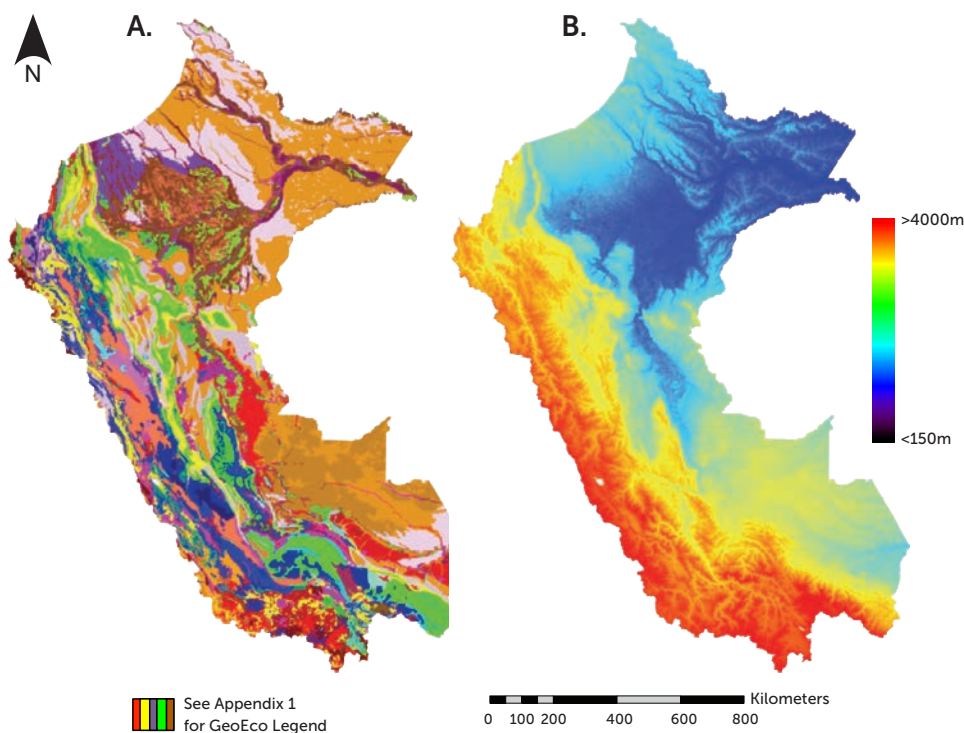


Figure 19

(A) Pre-stratification of the airborne sampling region using a new combination of geological, soil, and floristic compositional maps. (B) Topography of the airborne sampling region from NASA Shuttle Radar Topography Mission (SRTM) data.

LiDAR Data Acquisition

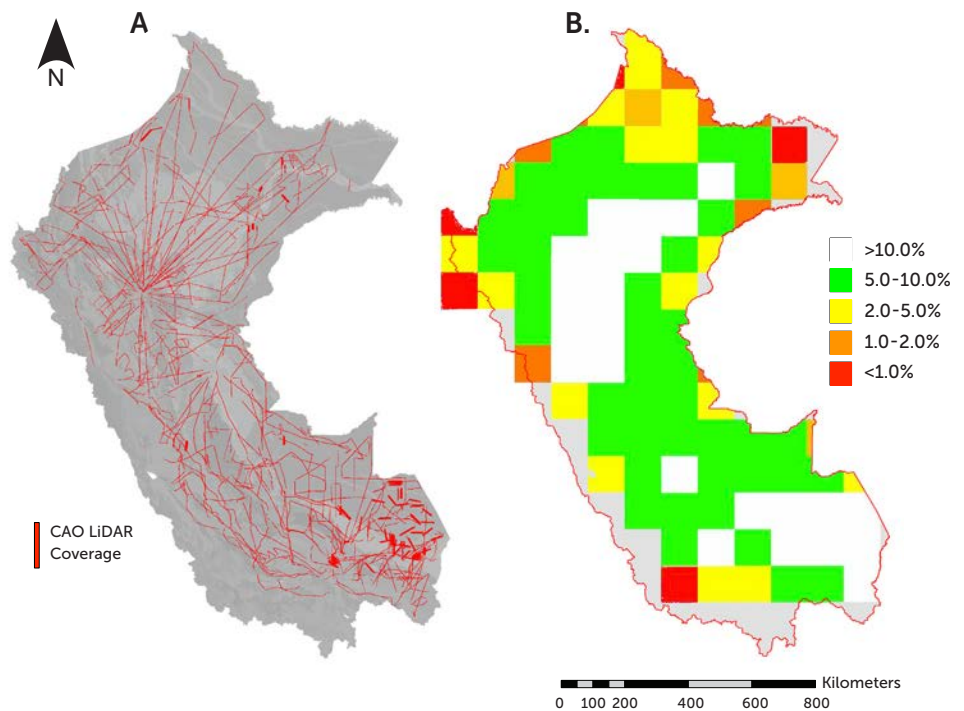
The LiDAR data were collected using the Carnegie Airborne Observatory-2 Airborne Taxonomic Mapping System (AToMS; ⁵⁸), which is carried onboard a twin turbopropeller Dornier 228 aircraft. The AToMS LiDAR is a dual laser, scanning waveform system capable of firing at 500,000 laser shots per second. To cover the maximum area per flight hour, the aircraft was operated at speeds of up to 150 knots at an altitude averaging 2000 m above ground level. The

LiDAR settings were configured to achieve an average on-the-ground laser spot spacing of 4 shots m^{-2} , peaking at 8 shots m^{-2} in areas of flightline overlap.

Airborne LiDAR sampling was carried out using 100 x 100 km grid cells overlaid on the GeoEcoElevation map. For this study, we sought to sample at least 2% (200 km^2) of each grid cell, with the additional goal of sampling at least 2% of the weighted contribution each GeoEcoElevation class to each grid cell. Past work has shown that 1% coverage per vegetation type yields robust and stable statistical distributions for landscapes of about 500 ha or larger²⁷. A total of 6,761,624 ha of LiDAR data were collected throughout the country in an extensive sampling pattern shown in **Figure 20A**. The LiDAR sampling density achieved by GeoEcoElevation class averaged 6.47% or 655.8 km^2 per grid cell (**Figure 20B**). Some grid cells to the far edges of the mapping area were sampled less, with the lowest forest cover amounting to 179.2 km^2 (1.8%) of a grid cell along the border with Colombia.

Figure 20

(A) Airborne Light Detection and Ranging (LiDAR) from the Carnegie Airborne Observatory is used to sample the region as shown in red lines. Total LiDAR observation coverage for this study was 6.7 million hectares. (B) Percentage coverage of each 100 x 100 km sampling grid cell. Previous studies indicate that over-sampling occurs at 1% LiDAR coverage, thus we consider this a "massive" sampling of the region.



LiDAR-based Canopy Height

Mean top-of-canopy height (TCH) was calculated for each hectare of LiDAR coverage ($n = 6,761,624$). To create this data layer, laser range measurements from the LiDAR were combined with embedded high resolution Global Positioning System-Inertial Measurement Unit (GPS-IMU) data to determine the 3-D locations of laser returns, producing a 'cloud' of LiDAR data. The resulting LiDAR data cloud consisted of a very large number of precisely georeferenced point elevation measurements ($n = \sim 278$ trillion), where elevation is relative to a reference ellipsoid (WGS 1984).

These LiDAR data points were processed to identify which laser pulses penetrated the canopy volume and reached the ground surface, from which a high-resolution digital terrain model (DTM) was developed. This was achieved

using a 10 m x 10 m filter kernel throughout the LiDAR coverage, and the lowest elevation in each kernel was deemed a possible ground detection. These filtered points were then evaluated by fitting a horizontal plane through each point. If the closest unclassified point was $< 5.5^\circ$ and < 1.5 m higher in elevation, the pre-filtered point was finalized as a ground-classified surface point. This process was repeated until all potential ground points within the LiDAR coverage were evaluated. A digital surface model (DSM), which is essentially the top-most surface (e.g., canopies, buildings, exposed ground), was also generated based on interpolations of all first-return points at 1.0 m spatial resolution. By combining the DTM and DSM in a tightly matched pair of data layers, the vertical difference between them yielded a high-accuracy model of top-of-canopy height (TCH) at 1.1 m spatial resolution throughout the 6,761,624 ha LiDAR sampling coverage. Previous validation studies of this CAO LiDAR TCH estimation approach has demonstrated it to be highly accurate in a wide range of forests including extremely densely foliated, tall tropical forests exceeding 60 m in height and leaf area index (LAI) levels^{59, 60}. The 1.1-m TCH data were then averaged to one-hectare resolution, which further decreases uncertainty in derived mean top-of-canopy canopy height⁶¹.

Upscaling LiDAR to a Full Map Coverage

Scaling up a large volume of LiDAR TCH data to full map coverage can be accomplished with a variety of techniques, one of which is applying LiDAR-derived statistics of canopy height to an environmental stratification map similar to our GeoEcoElevation map used for initial flight planning. Often stratification maps are based on *a priori* knowledge of vegetation type and/or abiotic factors such as soils, elevation, and climate. This “paint by numbers” stratified sampling approach is often used with plot-based forest inventory data to assign field-based estimates to different stratification classes⁶²⁻⁶⁴. Stratification has also been used with airborne LiDAR in nearly the same type of approach²⁷.

The problem with stratification is that it is overly dependent upon a *priori* knowledge of the factors that may or may not drive variation in the ecological metric of interest — aboveground carbon density in this case. In an environmentally complicated region like Perú, with ecosystems ranging from cold highland deserts to humid submontane assemblages to vast lowland forests on varying geologies, we likely cannot stratify well enough to develop confidence in bridging the scale gap from LiDAR or field plots to full geographic coverages. Moreover, because extremely large geographies contain exceedingly remote habitats and highly variable cloud densities, neither LiDAR datasets nor field inventory plots can be placed throughout them in a random or systematically-aligned design⁶⁵. This renders typical spatial methods for scaling, such as averaging or kriging¹⁴, prone to extremely large errors. As a result, maps based on stratification or simple spatial extrapolation are unreliable, and they cannot be used to properly generate spatially-explicit maps of uncertainty, which is paramount to understanding the stocks, gains and losses of carbon from a large, heterogeneous region such as the Peruvian Andes or the Amazon basin.

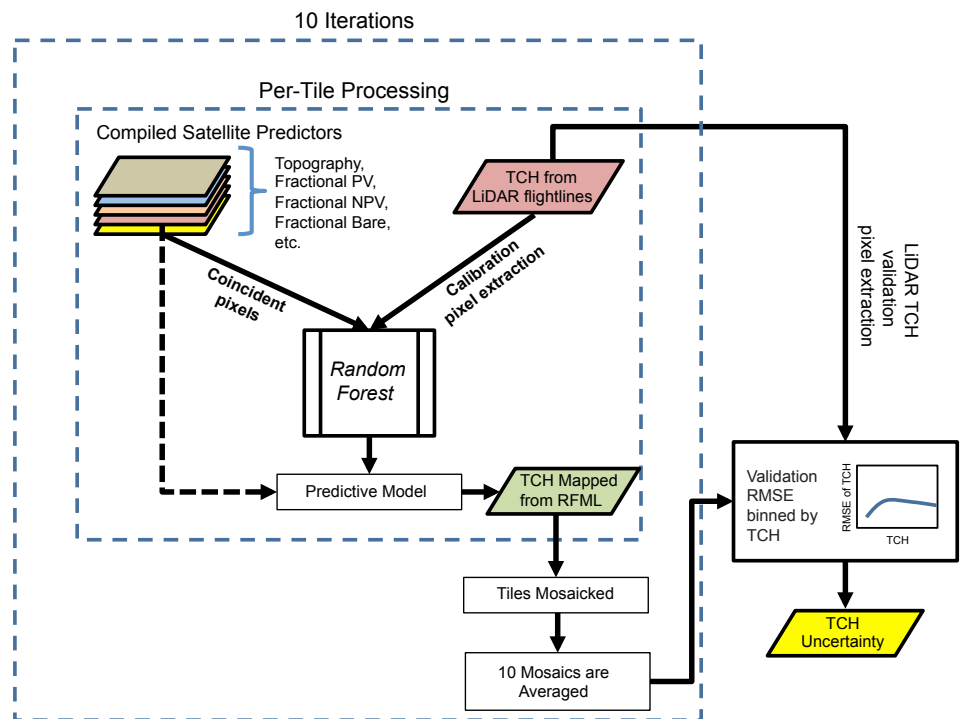
To meet this challenge, machine learning algorithms have been developed and applied to spatially-discontinuous datasets, like field plots and LiDAR sampling, in order to develop spatially-explicit estimates of vegetation properties based

on spatially-contiguous environmental variables such as topography, geologic substrate and long-term climate maps. In this context, the Random Forest Machine Learning (RFML) algorithm⁶⁶, has been used in global tropical forest carbon mapping², as well as in national, sub-national, and down-scaled global carbon mapping^{42, 49}. RFML fits multiple decision trees to input data (e.g. spatially-coincident environmental datasets) using a random subset of the input variables for each tree constructed for a given response variable (e.g., LiDAR TCH samples). The modal value of the calculated decision trees is used to create an “ensemble” tree that is used for prediction (e.g. spatially-contiguous TCH). RFML is non-parametric, insensitive to data skew, and robust to a high number of variable inputs⁶⁷. Recently, a comprehensive comparison of RFML to the traditional stratification-based approach for upscaling LiDAR samples has demonstrated the RFML approach in a 16 million ha portion of lowland Amazonia⁴⁸. However, that study also suggested that spatial context plays a major role in determining how well RFML can scale from local samples to full coverage, particularly with respect to strong gradients in environmental factors. In the case of the Andes-to-Amazon, or Perú as a whole, the region contains enormous variation in most abiotic factors including elevation, slope, aspect, geologic substrate and soils, floristics, and climate. Thus, RFML cannot perform well unless it has a mechanism to accommodate numerous and rapid spatial changes in environmental conditions.

To address this issue, we developed a new version of RFML based on a moving tile technique that ingests the airborne LiDAR data in local models (Figure 21). These tiles are then mosaicked together to form large, contiguous, national-scale mapping products. Specifically, we created hundreds of RFML models by dividing the LiDAR and environmental data into a system of geographic tiles, each covering 200 x 200 km per tile. In addition, we ran the models on these

Figure 21

New geostatistical modeling approach based on the Random Forest Machine Learning (RFML) algorithm. The country of Perú is gridded into 200 x 200 km cells. In each cell, a diverse set of compiled satellite predictor maps (Figure 22) are precisely co-aligned with airborne LiDAR samples. Up to 60,000 hectares of LiDAR data are randomly selected within a grid, and the RFML method is used to develop a prediction of LiDAR-based top-of-canopy height (TCH). This procedure is repeated ten times for each grid cell, with random selection of the input LiDAR data. An independent subset of LiDAR data are held back from the analysis of each grid cell to provide validation of the modeling results. This provides an estimate of the uncertainty in each grid cell.



tiles with an overlap of 50 km on each side, for a total coverage of 300 x 300 km per tile. In each tile, up to 60,000 1-ha LiDAR measurements of average TCH were randomly selected from all possible LiDAR 1-ha TCH values in the tile. The remaining unselected LiDAR data were used later for validation of the RFML modeling approach, described later.

The environmental variables used in each of the tiled RFML models were taken from co-aligned predictor spatial datasets (Figure 22). These include the fractional cover of photosynthetic vegetation (PV), non-photosynthetic vegetation (NPV), and bare substrate (Bare) derived from a national-scale mapping of Perú using the CLASlite approach with a mosaic of Landsat satellite imagery²². Each fractional cover map quantitatively indicates the percent cover of each surface material in every 30-m Landsat pixel, and as a result, the maps of PV, NPV and Bare substrate are highly sensitive to spatial variation in canopy gap fraction, openness and roughness, as described in previous

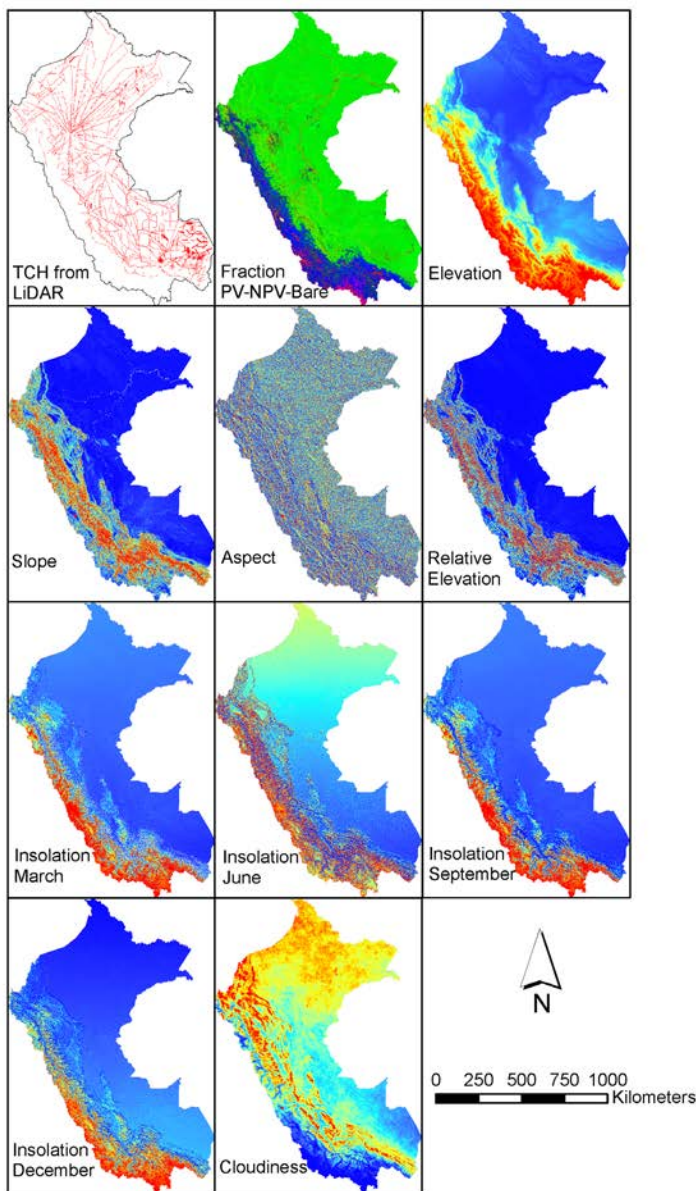


Figure 22

Geospatial datasets used in the Random Forest Machine Learning (RFML) algorithm to develop relationships between airborne LiDAR samples of top-of-canopy height (TCH; first image panel) and satellite-derived, continuous fields of fractional canopy cover (PV, NPV, Bare), topographic variables (elevation, slope, aspect, relative elevation above water body), average insolation at four points in the year, and cloudiness.

studies (e.g.,^{24, 37}). The fractional cover maps were computed from a mosaic of cloud-free imagery using the compositing method presented in Asner et al.⁴², with an additional cross-image brightness normalization⁵³. An additional set of environmental variables was derived from NASA Shuttle Radar Topography Mission (SRTM) at 90 m resolution: elevation, slope and aspect (Figure 22). A relative elevation model (REM) was also developed by calculating the height of the ground above nearest water body³⁰, thus providing a spatial proxy for vegetation-related water resources. We included multiple potential incoming solar insolation models using SRTM elevation data in the SAGA GIS Potential Insolation module⁶⁸. These insolation layers (units of kWhm⁻²) were created by modeling total insolation (direct and diffuse) for the days of the equinoxes and solstices (21st of Mar, Jun, Sept, and Dec). Additionally, we included long-term (2000-2010) cloudiness data derived from the NASA Moderate Resolution Imaging Spectroradiometer (MODIS). Cloudiness is based on the number of times a MODIS pixel was identified as being affected by clouds in the Quality Assurance (QA) flags of the 8-day reflectance product⁶⁹. The QA flags used in the compilation included the following: Pixel Adjacent to Cloud, Internal Cloud Algorithm, Cirrus Detected, Cloud Shadow and MOD35 Cloud. The number of flags that were set to "on" for each pixel were added and averaged to yield a percent cloudiness per pixel. All environmental predictor maps were resampled to one-hectare resolution, co-aligned, and combined into a stack of predictor variables covering the entire country of Perú.

The predictor maps and the LiDAR one-hectare TCH samples were run through the tile-based RFML models to create regression trees (Figure 1). Because the process was carried out on individual 300 x 300 km tiles, some discontinuities along the edges of each tile were observed. A mosaicking methodology was therefore developed to adjust the data in the overlap area of each tile in the mosaic. To accomplish this goal, a central tile was used as the start of the national-scale mosaic, and adjacent overlapping tiles were added one by one along the edges of the central tile. Each new tile added to the mosaic was adjusted as a weighted average of each pixel based on its proximity to the edge of the tile. For example, a one-hectare pixel on the very edge of a 300 x 300 km tile would be weighted more with the value of the overlapping pixel of its neighbor tile. Similarly, a pixel close to the center of its tile, but still in the overlap area, would be weighted more with the tile center to which it is closest.

To further increase the robustness of this tile-based RFML approach, we ran ten iterations for each tile, with each iteration randomly selecting a different set of up to 60,000 one-hectare LiDAR TCH observations. Additionally, in each tile RFML run, we successively shifted the extent of the tile by 10% (20 km) in the East-West and North-South directions. Each of these ten iterations formed a separate mosaic of the mapped (upscaled) TCH throughout Perú. The ten individual, national-scale mosaics were then averaged to produce a single national-scale map of TCH at one-hectare resolution, with a corresponding standard deviation map generated from the ten individual RFML modeling runs. The standard deviation map is an indicator of how uncertain predicted TCH is in each hectare of Perú based on using different sets of direct LiDAR TCH observations throughout the tiling system.

We left out 10.5% (536,874 ha) of the LiDAR data from the RFML models, randomly distributed throughout the entire LiDAR coverage. We used these data to validate the upscaled TCH map, which indicated a $R^2 = 0.78$ and a root

mean squared error (RMSE) of 3.50 m (Figure 23A). In addition, we analyzed our relative error in mapped TCH as a percentage RMSE against LiDAR-measured canopy height (Figure 23B). This indicated large relative errors of more than 60% on short (low biomass) vegetation of less than 5 m height, and decreasing relative error of less than 20% on higher biomass vegetation of 15 m or taller. For the purposes of ecological analysis or carbon accounting, these errors are quite low, and are heightened only in smaller canopies that often represent very low-biomass shrublands or rapidly regrowing successional vegetation associated with agricultural systems that are not large aboveground carbon stores. In contrast, our errors are demonstrably low for tall forest ecosystems where the overwhelming majority of aboveground carbon is stored.

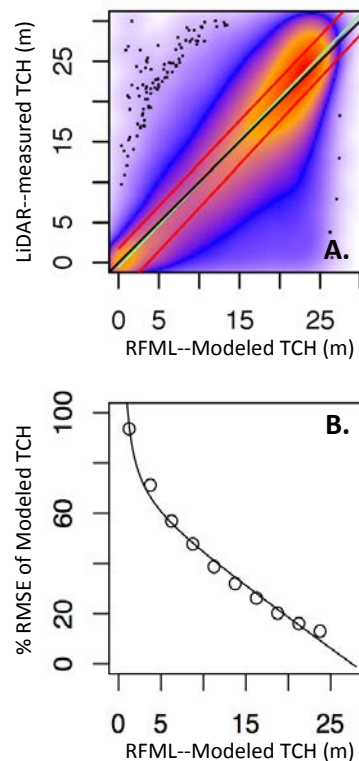


Figure 23

(A) Validation of top-of-canopy height (TCH) modeled at the national scale using the Random Forest Machine Learning (RFML) approach and direct measurements of TCH from airborne LiDAR. (B) Decline in uncertainty of RFML-based TCH estimates with increasing TCH. This result is critically important since the majority of aboveground carbon stock is associated with vegetation heights of 15 meters or more.

Calibrating Mapped TCH to ACD

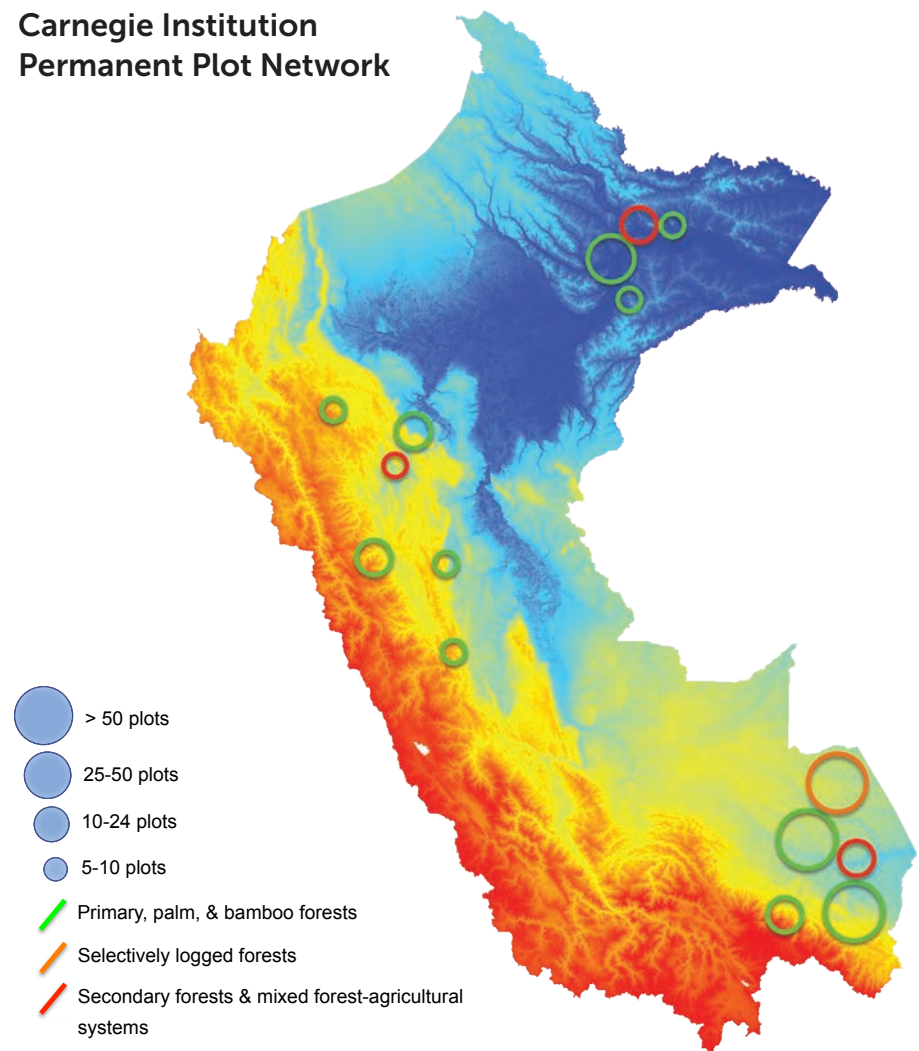
Aboveground carbon density (ACD) was estimated from the mapped TCH data following the approach of plot-aggregate allometric scaling^{43,44}. A highly precise and accurate link between TCH and field estimates of ACD can be made by applying regional plot-aggregated estimates of vegetation wood density and diameter-to-height relationships. To develop this TCH-to-ACD calibration for Andean and Amazonian forests, and other vegetation types throughout the region, a permanent inventory plot network was established in three latitudinal belts covering northern, central and southern Perú. The network includes 272 plots comprised of 262 0.3-hectare plots, and an additional 10 one-hectare plots as shown in Figure 24 (next page). The plot network is arranged in a nested design of 5-30 individual plots in 13 regionally distributed clusters to capture landscape-scale heterogeneity in carbon stocks across geological, soil, topographic and floristic compositional conditions. The plots include major forest types in lowland Amazonia including white sand, clay terrace, alluvial floodplain, swamp, *Mauritia* palm and bamboo-dominated ecosystems. Additionally, the plot network incorporates an extensive sampling of submontane and montane dry to wet forests, woodlands and shrublands up to treeline at multiple altitudes and latitudes. Finally, the plot network includes coverage of both primary and secondary forests, selectively logged forests, Brazil-nut concession forests, and highly degraded to deforested lands.

We estimated ACD in each field plot using allometric models. We first accounted for dead trees and non-tree growth forms, such as palms, bamboo, and lianas, by using growth-form-specific allometric models²⁷. For palms and dead trees we used models incorporating height measured using laser range finders. For all other individuals, we used a new, generalized allometric

Figure 24

Regional distribution and density of Carnegie permanent field plot network in Perú. Circle locations indicate the centroid of each cluster of inventory plots; Circle colors indicate general forest type and condition; Elevation map indicates the partitioning of plots in lowland (blue-green), submontane (yellow) and montane (red) conditions.

Carnegie Institution Permanent Plot Network



model from Chave et al.¹⁸, which in addition to diameter, requires inputs of wood density and height. We identified 98.7% of living stems to genus, and obtained a genera-specific wood density estimate from a global wood density database for 96.4% of living stems. We accounted for height variation using a combination of direct measurements (with either laser range finders or clinometers) and diameter-based estimation. We measured the height of the three largest-diameter trees in each plot (e.g., those with the greatest importance to carbon estimation) as well as seven or more additional trees in each plot spanning a range of diameters. These tree height data were used in two ways: (a) measured trees retained their measured heights for input into the Chave et al.¹⁸ allometric model, and (b) more than 10,400 tree measurements were used for the creation of a diameter-to-height model that was used to estimate the height of all other trees. We multiplied all dry biomass estimates by 0.48 to calculate ACD

We used maximum likelihood analysis to fit a power-law model between field-estimated ACD and TCH. The fit was performed on the un-transformed TCH and ACD values using a non-arithmetic error term to account for heteroskedasticity; this method is analogous to fitting a linear model to

the log-transformed TCH and ACD data, but avoids the need for back-transformation⁷⁰. In addition, a recently identified change in wood density with elevation was incorporated into the TCH-to-ACD calibration using plots along an Andean-Amazon elevation gradient⁷¹, thereby establishing the regression slope of a linear relationship between wood density and elevation. This slope was found to be 0.00005 mg cm⁻³ m⁻¹ of elevation gain above 400 m elevation. The adjustment was applied to plots of elevations above 400 m:

$$WD_{adj} = WD_{orig} + ((ELEV_{site} - 400) * 0.00005) \quad (i)$$

Incorporating this adjustment for the elevation-dependence of wood density, the average increase in ACD at 1-ha resolution was 5.0 Mg ha⁻¹ or 5.24%. The resulting relationship between TCH and ACD is shown in **Figure 25**, with an RMSE = 27.4 Mg C ha⁻¹ and an R² = 0.82. We view this accuracy and precision as excellent given the extreme breadth of vegetation structural, floristic and land-use variation incorporated in our permanent plot network (**Figure 25**). The final calibration equation relating top-of-canopy height (TCH) to aboveground carbon density (ACD) for Andean and Amazonian forests is:

$$ACD = 0.8245 \times TCH^{1.573} \quad (2)$$

This equation was applied to the Perú-wide TCH map generated from the Random Forest modeling.

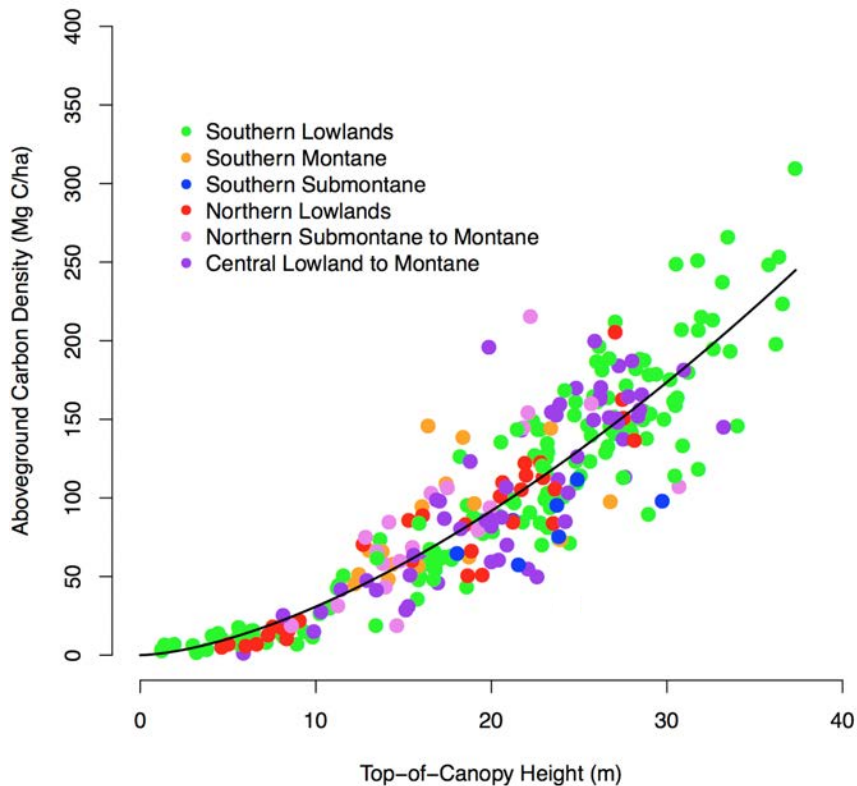


Figure 25

Calibration of airborne LiDAR-based measurements of top-of-canopy height (TCH) against field-based estimates of aboveground carbon density (ACD) in lowland, submontane and montane vegetation throughout Perú.

Validation of Mapped Carbon Densities

To validate the accuracy of our final carbon map, we held back field-based ACD estimates from 43 plots spread throughout the permanent plot network coverage. In addition, we used the eight RAINFOR plots spread throughout lowland Amazonia⁷² and six sub-montane and montane plots⁷³ available in the literature. These field plot-based estimates of ACD were regressed against one-hectare mapped estimates from the RFML modeling. The results of this validation are shown in **Figure 4**.

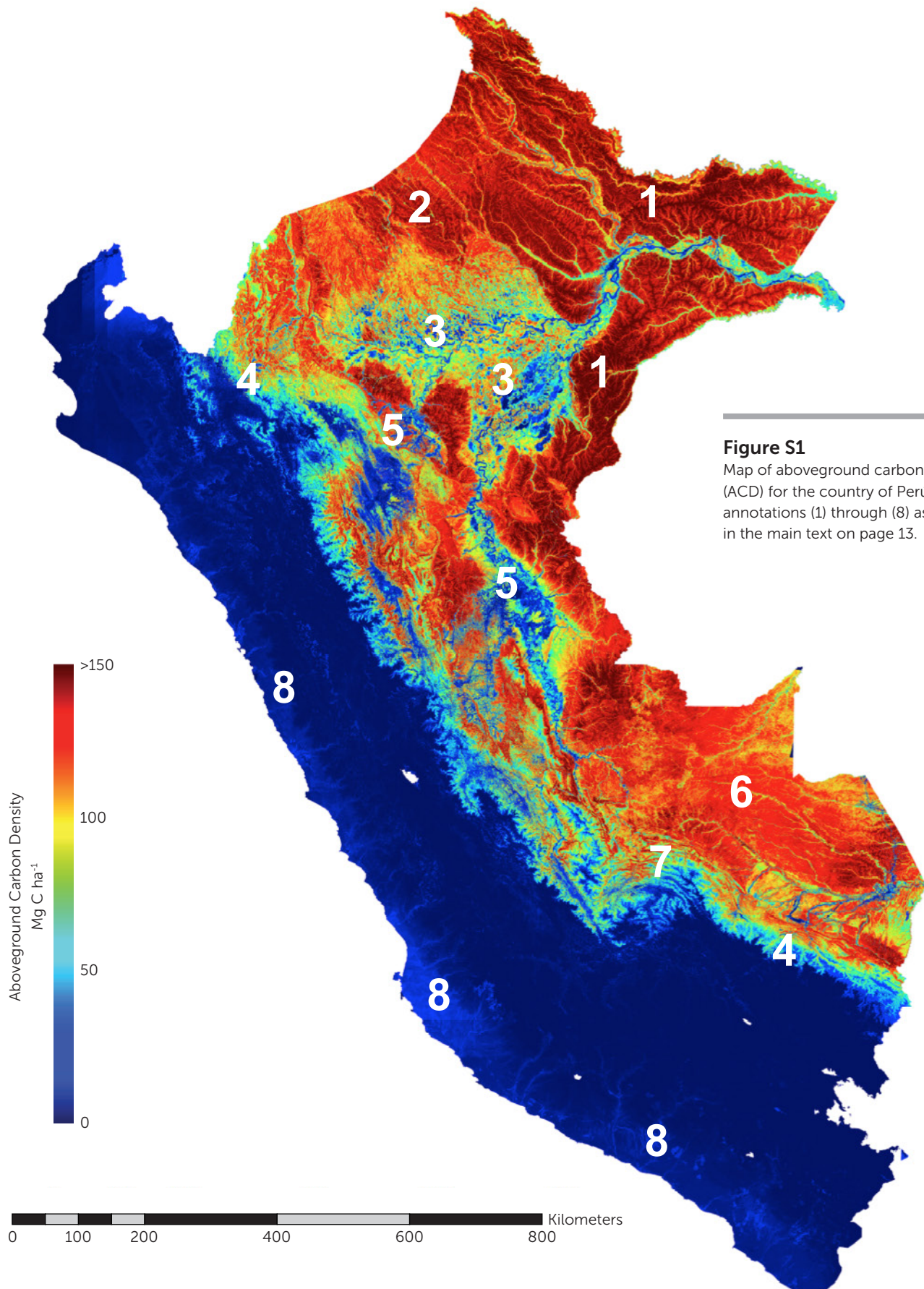


Figure S1

Map of aboveground carbon density (ACD) for the country of Perú, with annotations (1) through (8) as discussed in the main text on page 13.

Figure S2

Zoom images of aboveground carbon density (ACD) to highlight natural sources of extreme variation, such as (A) Amazon river floodplain dynamics; (B) Prevalence of bamboo in Southern Peruvian Amazon forests; and (C) Dissipation of carbon stocks toward treeline in the Andes.

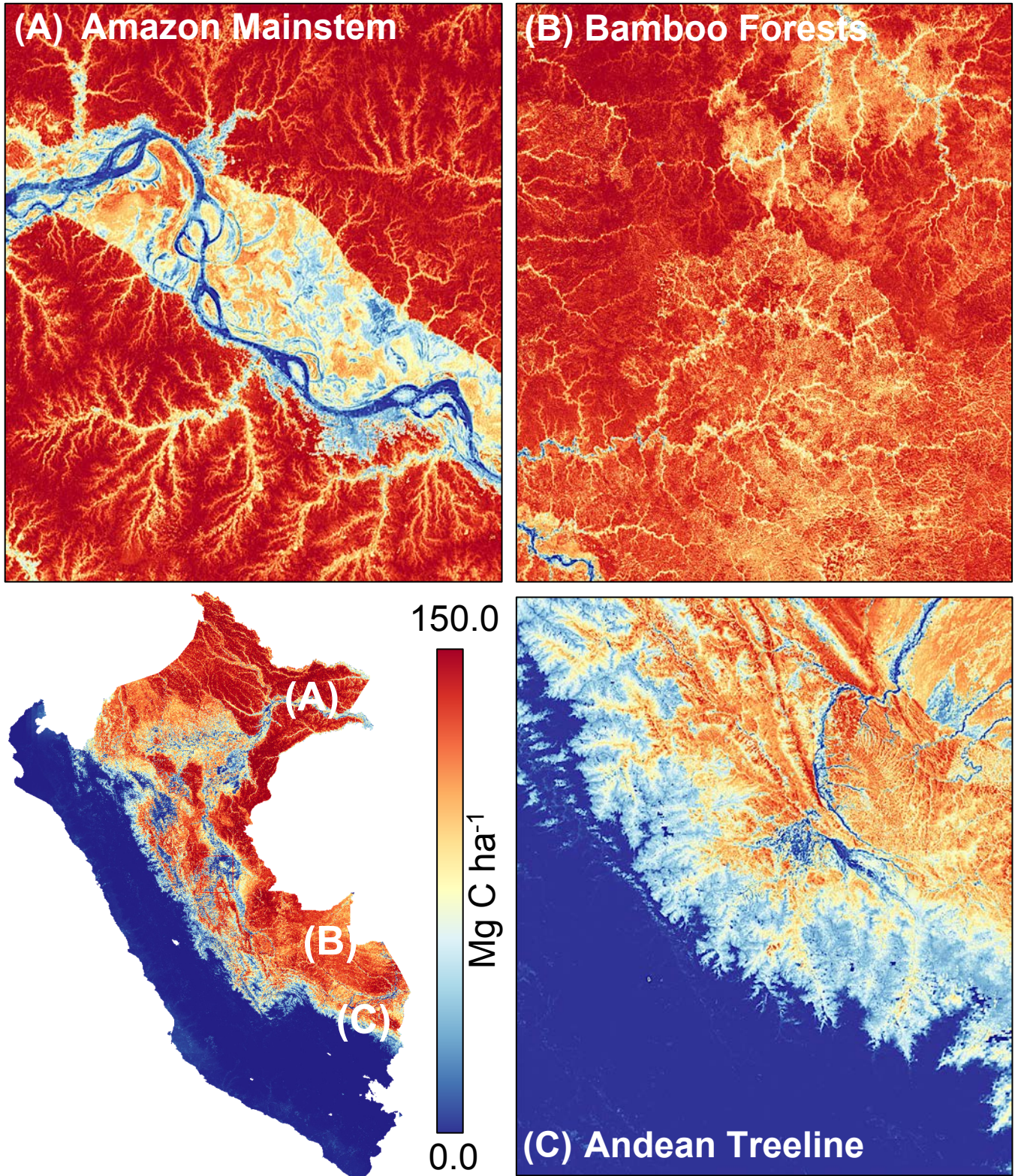


Figure S3

Zoom images of aboveground carbon density (ACD) to highlight human-dominated sources of variation, such as (A) Deforestation and forest degradation around the city of Puerto Maldonado in Madre de Dios; (B) Deforestation along the Iquitos-Nauta road in Loreto; and (C) Massive areas of deforestation and land conversion outside of the city of Pucallpa in Ucayali.

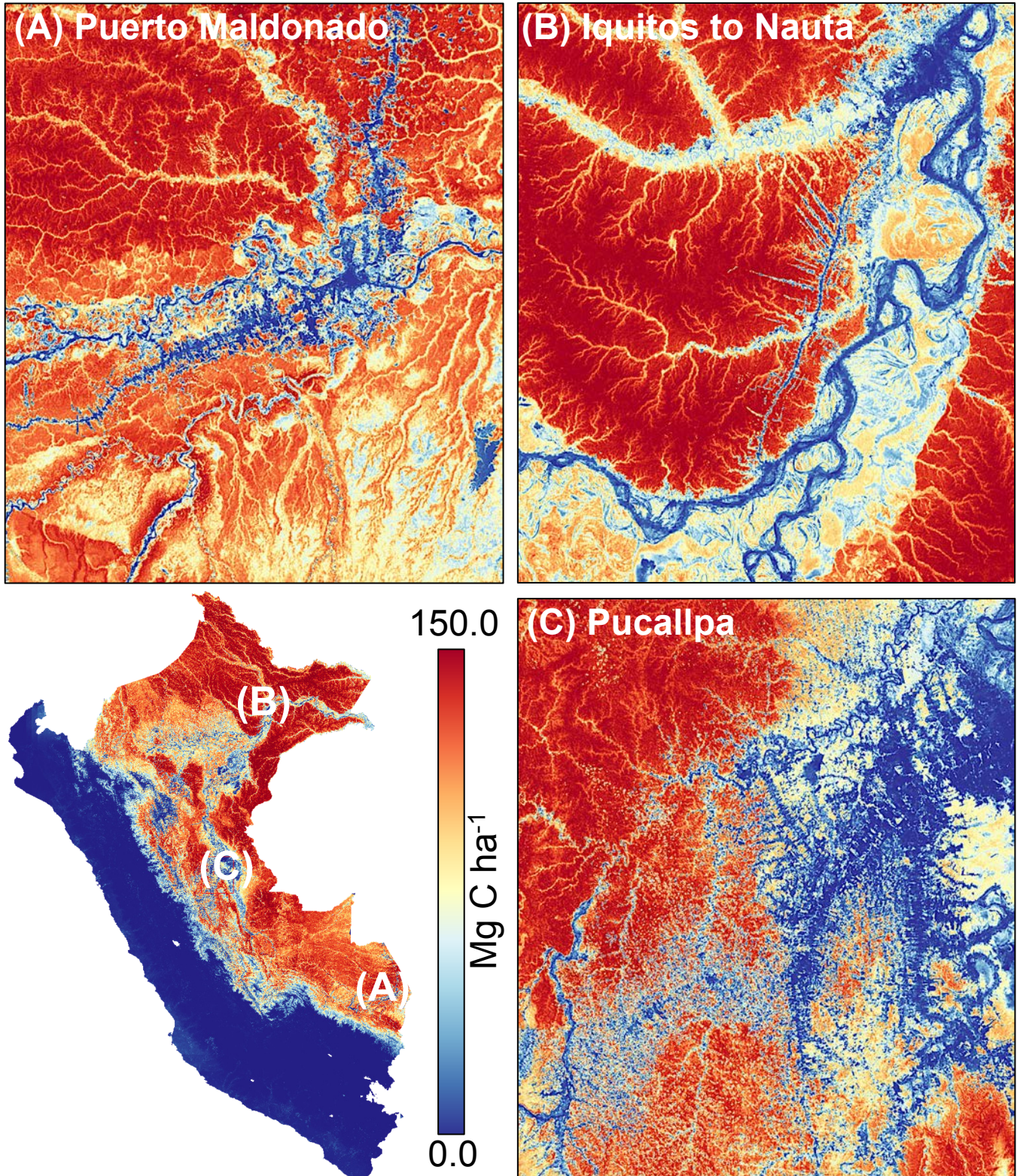
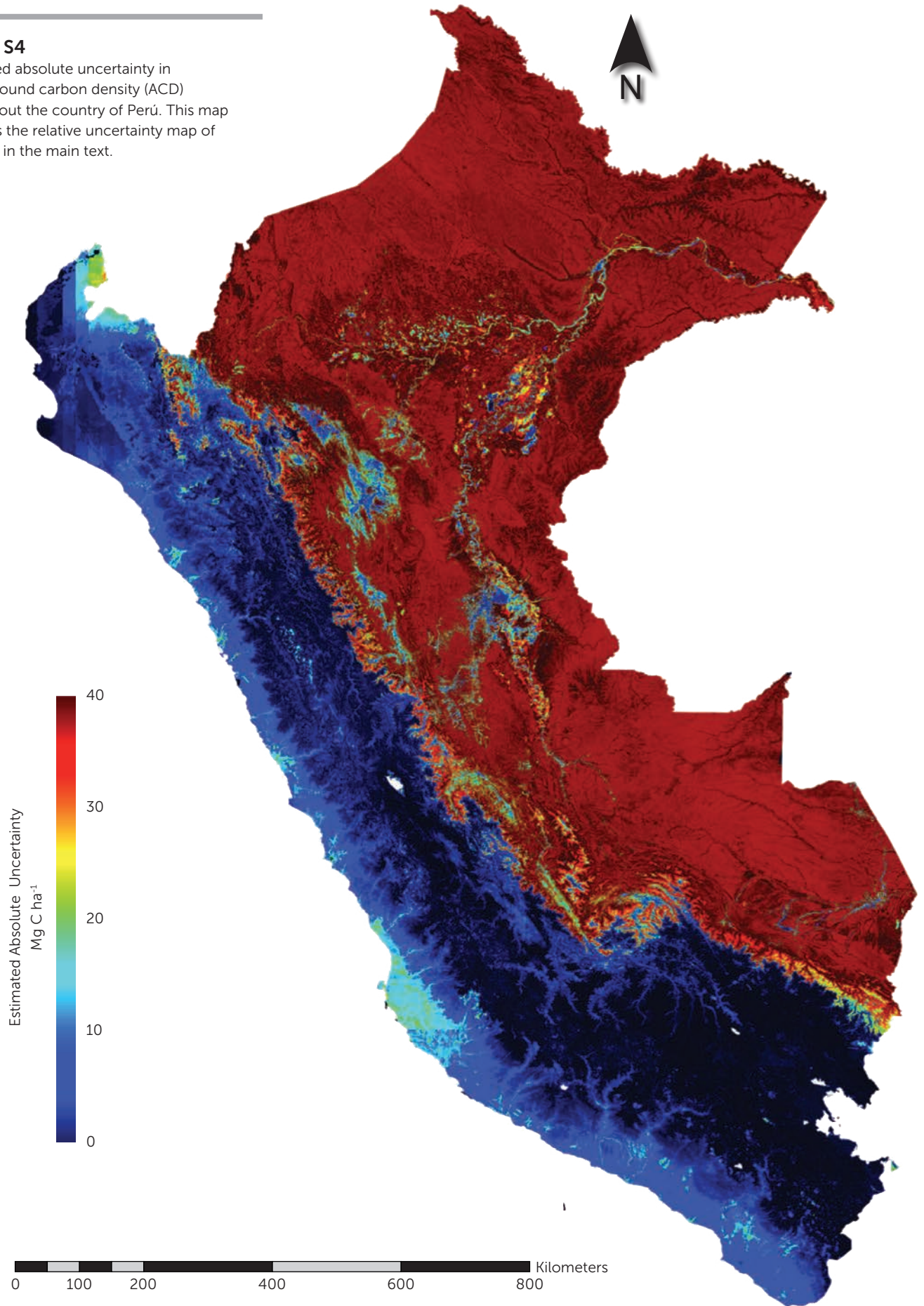


Figure S4

Estimated absolute uncertainty in aboveground carbon density (ACD) throughout the country of Perú. This map matches the relative uncertainty map of Figure 3 in the main text.



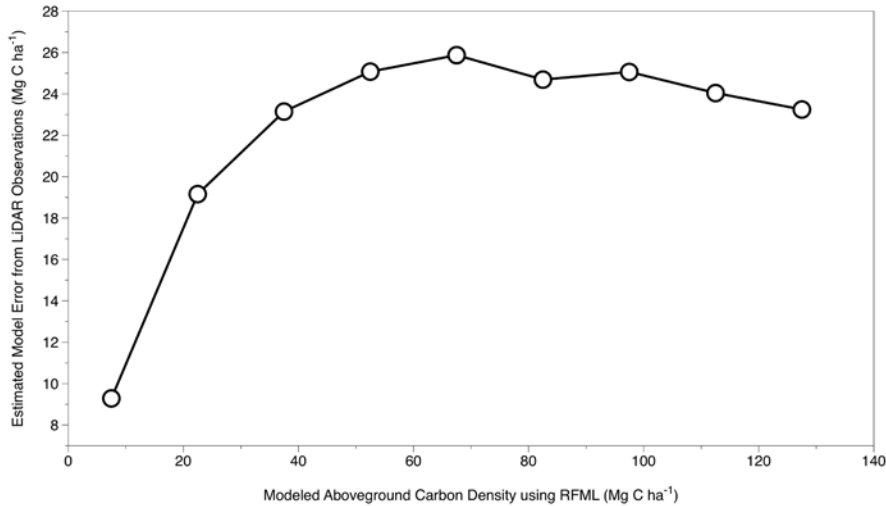


Figure S5

Uncertainty of aboveground carbon density (ACD) mapped at the national scale expressed as root mean squared error (RMSE) of LiDAR-estimated ACD.

Appendix Table 1

Codes and descriptors of geological-ecological classes used as input to the development of the "GeoEcoElevation" map (Figure 19) for airborne LiDAR flight planning. This table is intentionally presented in Spanish to most closely match the Peruvian government's Geological Map of Peru nomenclature.

Geo-Eco Code	Descriptor
Ci-c	Carbonifero inferior continental
Ci-c Bamboo	Carbonifero inferior continental Bamboo
CsP-m	Carbonifero superior-Permico
CsP-m Bamboo	Carbonifero superior-Permico Bamboo
CsP-v	Carbofinero sup.Permico volc-sed.
D-m	Devonico marino.
D-m Bamboo	Devonico marino. Bamboo
Dc-mzg/gr	Devonico Plutones Eohercinicos
Dc-to/gd	Plutones Eohercinicos
Domos	Domos
E-ms	Cambrico marino-sedimentario.
Ji-vs	Jurasico inferior volc-sedimentario.
Jm-m	Jurasico medio marino.
Js-c	Jurasico superior continental.
Js-m	Jurasico sup.marino
Js-to/gd/di	Plutones Cord. del Condor
JsKi-mc	Jurasico sup.-Cretaceo inf.marino-cont.
JsKi-vs	Jurasico sup.-cretaceo inf.volc-sed.
Ki-c	Cretaceo inferior continental
Ki-c Bamboo	Cretaceo inferior continental Bamboo
Ki-m	Cretaceo Inf.Marino.
Ki-mc	Crteaceo inf.Marino Continental
Ki-mc Bamboo	Crteaceo inf.Marino Continental Bamboo
Kis-m	Cretaceo inf.sup.Marino.
Kis-m Bamboo	Cretaceo inf.sup.Marino. Bamboo
KP-to/gd	Cretaceo Paleg.ton/gd.
Ks-c	Cretacio superior continental.
Ks-c Bamboo	Cretacio superior continental. Bamboo

Geo-Eco Code	Descriptor
Ks-mc	Cretaceo Sup.marino continental
KsP-c	Cretacio sup. Paleogeno continental.
Lagunas	Lagunas.
N-an/ri	Neogeno andesita- riolitia
N-f	Neogeno
N-gd/to	Neogeno granodirita-tonalita.
New01	Pleistocene Alluvial Terrace
New02	Upper Pastaza Fan
Nm-c	Neogeno mioceno-continental
Nm-v	Neogeno mioceno-volcanico
Nm-vs	Neogeno mioceno volc-sedimentario.
Nmp-c	Neogeno mioceno-continental.
Nmp-c Bamboo	Neogeno mioceno-continental. Bamboo
Nmp-v	Neogeno mioceno plioceno-volcanico.
Nmp-vs	Neogeno mioceno plioceno-volc sedimentar
Np-v	Neogeno plioceno-volcanico
Np-vs	Neogeno plioceno-volc sedimentario.
NQ-c	Neogeno Cuaternario-continental.
NQ-c Bamboo	Neogeno Cuaternario-continental. Bamboo
NQ-v	Neogeno Cuaternario-volcanico.
O-ms	Ordovico-metasedimento
P-an/ri	Cuerpos Subvolcanicos
P-c	Paleoceno continental
P-c Bamboo	Paleoceno continental Bamboo
P-to/gd	Tonalitas y granodioritas paleogenas
Pali-ms	Metased. del Paleozoico
Pe-m	Paleogeno eoceno marino
Pe-vs	Paleogeno eoceno volcanico-sedimentario.
PeA-e/gn	Precambrico
PeA-gn	Precambrico neoproterozoico gneis.
Pi-gd/gr	Paleozoico inf.granod-granito.
Pis-mc	Permico
Pis-mc Bamboo	Permico Bamboo
PN-c	Paleogeno-Neogeno Continental
PN-c Bamboo	Paleogeno-Neogeno Continental Bamboo

Geo-Eco Code	Descriptor
PN-gd/to	Batolito de Abancay
PN-vs	Paleogeno Neogeno Volc.Sed.
Po-m	Paleogeno oligoceno mioceno
Pp-c	Paleogeno-Paleoceno continental.
Pp-vs	Paleogeno Paleoceno Volc.Sed.
Ps-c	Permico superior continental.
PT-mzg/gr	Plutones Tardihercinicos
PT-to/gd	Permico Plutones Tardihercinicos
Qh-c	Cuaternario holoceno-continental.
Qh-c Bamboo	Cuaternario holoceno-continental. Bamboo
Qpl-c	Cuaternario pleistoceno continental
Qplh-v	Cuaternario plioceno holoceno volc.
SD-ms	Silurico-Devonico metasedimento
TsJi-m	TriasicoSup Jurasico inf.marino
DF-100	Areas Antropicas
100 Bamboo	Areas Antropicas Bamboo
DF-99	Cuerpos de Agua
CES408.523	Bosque siempreverde de la penillanura del oeste de la Amazonia
CES408.523 Bamboo	Bosque siempreverde de la penillanura del oeste de la Amazonia Bamboo
CES408.526	Bosque aluvial de aguas negras estancadas del sur de la Amazonia
CES408.526 Bamboo	Bosque aluvial de aguas negras estancadas del sur de la Amazonia Bamboo
CES408.528	Bosque de arroyos de aguas claras del suroeste de la Amazonia
CES408.531	Bosque inundable de la llanura aluvial de rios de aguas blancas del suroeste de Zona de Reservada
CES408.531 Bamboo	Bosque inundable de la llanura aluvial de rios de aguas blancas del suroeste de Zona de Reservada
CES408.532	Bosque inundable de la llanura aluvial de rios de aguas blancas del oeste de la
CES408.535	Bosque inundable y vegetacion riparia de aguas negras del suroeste de la Amazonia
CES408.536	Bosque inundable y vegetacion riparia de aguas negras del oeste de la Amazonia
CES408.538	Bosque pantanoso de palmas de la llanura aluvial del oeste de la Amazonia
CES408.543	Bosque siempreverde subandino del suroeste de la Amazonia
CES408.543 Bamboo	Bosque siempreverde subandino del suroeste de la Amazonia Bamboo
CES408.544	Bosque siempreverde estacional de la penillanura del suroeste de la Amazonia
CES408.544 Bamboo	Bosque siempreverde estacional de la penillanura del suroeste de la Amazonia Bamboo
CES408.545	Bosque siempreverde estacional subandino del suroeste de la Amazonia
CES408.546	Bosque azonal semideciduo de colinas del oeste de la Amazonia
CES408.548	Bosque de serranias aisladas del oeste de la Amazonia
CES408.549	Bosque con Bambu del suroeste de la Amazonia
CES408.549 Bamboo	Bosque con Bambu del suroeste de la Amazonia Bamboo
CES408.550	Complejo de vegetacion sucesional riparia de aguas blancas de la Amazonia

Geo-Eco Code	Descriptor
CES408.550 Bamboo	Complejo de vegetacion sucesional riparia de aguas blancas de la Amazonia Bamboo
CES408.552	Herbazal pantanoso de la llanura aluvial de la alta Amazonia
CES408.560	Sabanas arboladas y arbustivas de la alta Amazonia sobre suelos anegables
CES408.562	Vegetacion escler?fila de arenas blancas del oeste de la Amazonia
CES408.565	Bosque siempreverde subandino del oeste de la Amazonia
CES408.569	Bosque pantanoso de la llanura aluvial del oeste de la Amazonia
CES408.569 Bamboo	Bosque pantanoso de la llanura aluvial del oeste de la Amazonia Bamboo
CES408.570	Bosque del piedemonte del suroeste de la Amazonia
CES408.570 Bamboo	Bosque del piedemonte del suroeste de la Amazonia Bamboo
CES408.571	Bosque inundable y vegetacion riparia de aguas mixtas de la Amazonia
CES408.572	Bosque del piedemonte del oeste de la Amazonia
CES408.573	Bosque pantanoso de palmas de la llanura aluvial del sur de la Amazonia
CES408.573 Bamboo	Bosque pantanoso de palmas de la llanura aluvial del sur de la Amazonia Bamboo
CES408.574	Bosque inundable de la llanura aluvial de rios de aguas negras del centro-sur de
CES408.576	Bosque de tierra firme depresionada del sur de la Amazonia
CES408.578	Bosque inundado por aguas blancas estancadas del suroeste de la Amazonia
CES409.039	Arbustal y herbazal sobre mesetas subandinias orientales
CES409.043	Bosque altimontano pluvial de Yungas
CES409.044	Bosque altimontano pluviestacional de Yungas
CES409.048	Bosque y palmar basimontano pluvial de Yungas
CES409.050	Bosque montano pluvial de Yungas
CES409.053	Bosque basimontano pluviestacional subh-medio de Yungas del sur
CES409.054	Bosque basimontano pluviestacional h-medio de Yungas
CES409.056	Bosque basimontano xerico de Yungas del sur
CES409.057	Matorral xerico interandino de Yungas
CES409.058	Pajonal arbustivo altoandino y altimontano pluvial de Yungas
CES409.059	Pajonal arbustivo altoandino y altimontano pluviestacional de Yungas
CES409.061	Palmar pantanoso subandino de Yungas
CES409.062	Sabana arbolada montana y basimontana de Yungas
CES409.075	Bosque y arbustal montano xerico interandino de Yungas
CES409.079	Bosque y arbustal basimontano xerico de Yungas del norte
CES409.914	Bosque pluvial sobre mesetas de la Cordillera del Condor
CES409.921	Bosque montano pluviestacional subh-medio de Yungas
Co01Amazonia	Complejo de sabanas del sur de la Amazonia
Co02Amazonia	Complejo de bosques sucesionales inundables de aguas blancas de la Amazonia
Co02Andes	Complejo submontano seco de Yungas del norte

We thank Guayana Páez Acosta and John Clark for outstanding coordination of the Carnegie-MINAM team. We thank Loreli Carranza-Jimenez, James Jacobson, Nestor Jaramillo, Ty Kennedy-Bowdoin, Paola Martinez, Paola Perez, Kelly Salcedo, Elif Tasar, Eloy Victoria and many others for their dedication and contributions to this study. We thank Deborah Bigio, Margaret Copeland, Chris Field, and Marion O’Leary for their contributions to this effort and the resulting report. We thank Steve Cornelius, Paulina Arroyo, Luis Solórzano, and Jorgen Thomsen for believing in our science and capacity building approach.

We sincerely thank the Peruvian Ministry of Environment for its sustained collaboration and support, and the Peruvian Air Force for logistical assistance. We acknowledge the following Peruvian agencies for research authorizations that made this study possible: Direccion General Forestal y Fauna Silvestre RD N° 007-2012-AG-DGFFS-DGEFFS and RD N°0187-2013-AG-DGFFS-DGEFFS; Reserva Nacional Allpahuayo Mishana RJ N° 001-2012-SERNANP-RNAM-J; ACR-Cordillera Escalera RJ-ACR-CE N° 10-2012/GRSM/PEHCNM/DMA/ACR-CE, Parque Nacional Tingo Maria RJ N° 01-2014-SERNANP-DGANP-PNTM; and Parque Nacional Yanachaga Chemillen N° 002-2014-SERNANP-DGANP-JEF.

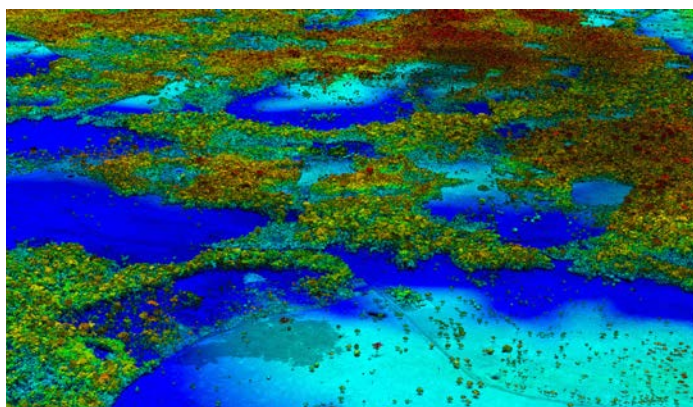
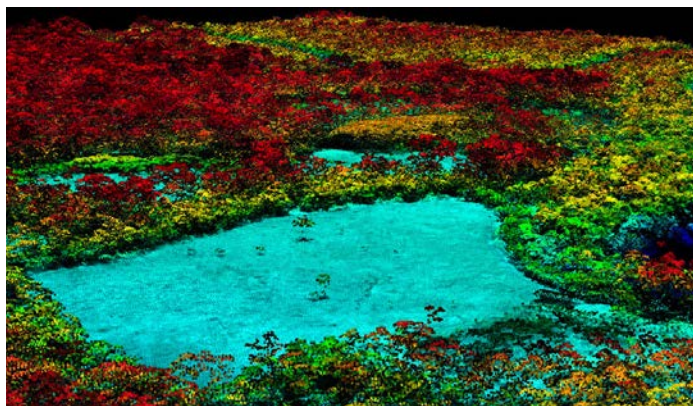
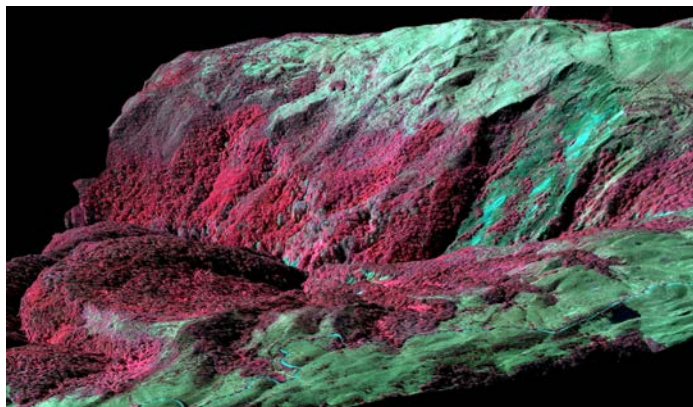
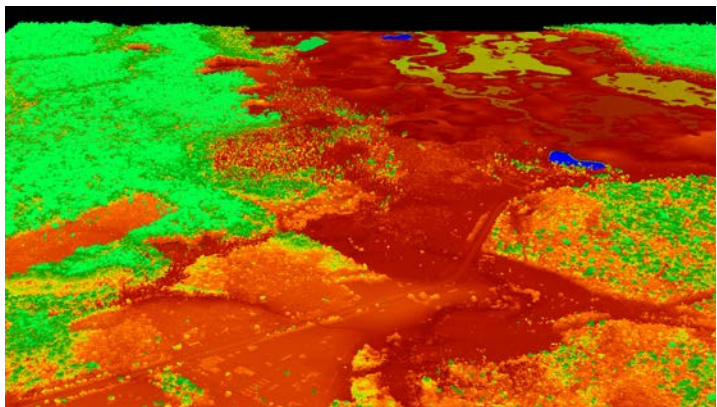
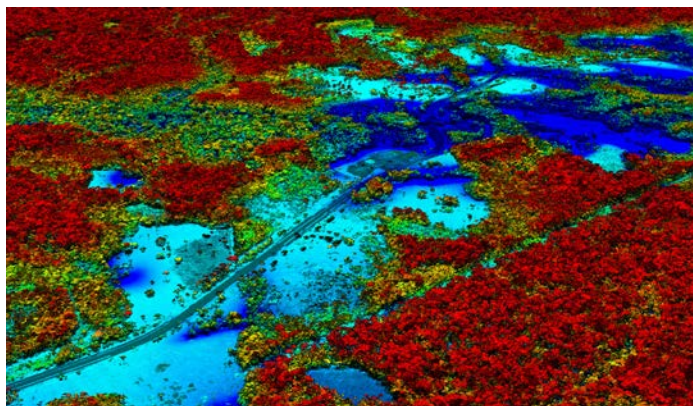
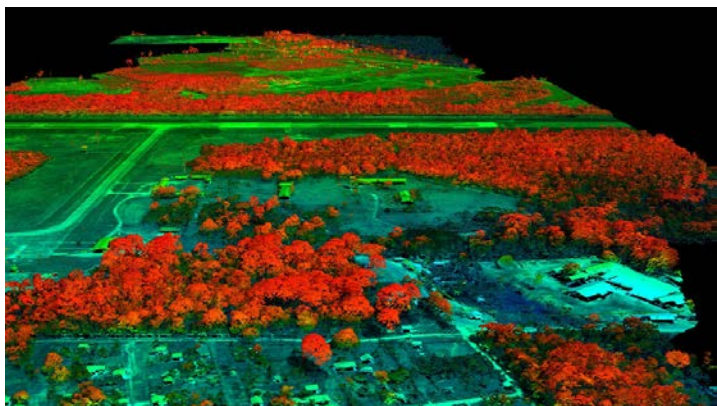
This conservation, land-use and climate change project was supported by the John D. and Catherine T. MacArthur Foundation, Gordon and Betty Moore Foundation, and the Carnegie Institution for Science. The Carnegie Airborne Observatory is made possible by the unique support of the Avatar Alliance Foundation, Grantham Foundation for the Protection of the Environment, John D. and Catherine T. MacArthur Foundation, Gordon and Betty Moore Foundation, W. M. Keck Foundation, Margaret A. Cargill Foundation, Mary Anne Nyburg Baker and G. Leonard Baker Jr., and William R. Hearst III.

1. Angelsen A (2008) *Moving Ahead with REDD: issues, options and implications* (Center for International Forestry Research (CIFOR), Bogor, Indonesia) p 156p.
2. Baccini A, *et al.* (2012) Estimated carbon dioxide emissions from tropical deforestation improved by carbon-density maps. *Nature Clim. Change* doi:10.1038/nclimate1354.
3. Pelletier J, Ramankutty N, & Potvin C (2011) Diagnosing the uncertainty and detectability of emission reductions for REDD + under current capabilities: an example for Panama. *Environmental Research Letters* 6(2):024005.
4. REDD-Offset-Working-Group (2013) California, Acre and Chiapas: Partnering to reduce emissions from tropical deforestation. ed Johnson E (Green Technology Leadership Group, Sacramento, CA USA), p 69.
5. Newell RG & Stavins RN (2000) Climate Change and Forest Sinks: Factors Affecting the Costs of Carbon Sequestration. *Journal of Environmental Economics and Management* 40(3):211-235.
6. IBWM (2006) The International Systems of Units. ed Measures IBoWa (Organisation Intergouvernementale de la Convention du Metre, Paris, France), p 186.
7. Lindenmayer DB, Laurance WF, & Franklin JF (2012) Global decline of large old trees. *Science* 338(6112):1305-1306.
8. Lugo AE & Scatena FN (1996) Background and catastrophic tree mortality in tropical moist, wet, and rain forests. *Biotropica* 28(4, part A):585-599.
9. Asner GP (2013) Geography of forest disturbance. *Proceedings of the National Academy of Sciences*.
10. Malhi Y, *et al.* (2006) The regional variation of aboveground live biomass in old-growth Amazonian forests. *Global Change Biology* 12(7):1107-1138.
11. Alves LF, *et al.* (2010) Forest structure and live aboveground biomass variation along an elevational gradient of tropical Atlantic moist forest (Brazil). *Forest Ecology and Management* 260(5):679-691.
12. Baraloto C, *et al.* (2011) Disentangling stand and environmental correlates of aboveground biomass in Amazonian forests. *Global Change Biology* 17(8):2677-2688.
13. Mitchard E, *et al.* (2013) Uncertainty in the spatial distribution of tropical forest biomass: a comparison of pan-tropical maps. *Carbon Balance and Management* 8(1):10.
14. Mitchard ETA, *et al.* (2014) Markedly divergent estimates of Amazon forest carbon density from ground plots and satellites. *Global Ecology and Biogeography*:n/a-n/a.
15. Chave J, *et al.* (2005) Tree allometry and improved estimation of carbon stocks and balance in tropical forests. *Oecologia* 145:87-99.
16. Clark DB & Kellner JR (2012) Tropical forest biomass estimation and the fallacy of misplaced concreteness. *Journal of Vegetation Science* 23(6):1191-1196.
17. Asner GP, Llactayo W, Tupayachi R, & Luna ERe (2013) Elevated rates of gold mining in the Amazon revealed through high-resolution monitoring. *Proceedings of the National Academy of Sciences* 110(46):18454-18459.
18. Chave J, *et al.* (2014) Improved allometric models to estimate the aboveground biomass of tropical trees. *Global Change Biology*:doi:10.1111/gcb.12629.
19. Colgan MS, Asner GP, & Swemmer T (2013) Harvesting tree biomass at the stand-level to assess the accuracy of field and airborne biomass estimation in savannas. *Ecological Applications* 23:1170-1184.
20. Asner GP & Heidebrecht KB (2002) Spectral unmixing of vegetation, soil and dry carbon cover in arid regions: comparing multispectral and hyperspectral observations. *International Journal of Remote Sensing* 23(19):3939-3958.

21. Asner GP, Bustamante MMC, & Townsend AR (2003) Scale dependence of biophysical structure in deforested areas bordering the Tapajós National Forest, Central Amazon. *Remote Sensing of Environment* 87(4):507-520.
22. Asner GP, Knapp DE, Balaji A, & Paez-Acosta G (2009) Automated mapping of tropical deforestation and forest degradation: CLASlite. *Journal of Applied Remote Sensing* 3:033543.
23. Asner GP, Archer S, Hughes RF, Ansley RJ, & Wessman CA (2003) Net changes in regional woody vegetation cover and carbon storage in Texas drylands, 1937-1999. *Global Change Biology* 9(3):316-335.
24. Carlson KM, *et al.* (2012) Committed carbon emissions, deforestation, and community land conversion from oil palm plantation expansion in West Kalimantan, Indonesia. *Proceedings of the National Academy of Sciences* 109(19):7559-7564.
25. Koltunov A, Ustin SL, Asner GP, & Fung I (2009) Selective logging changes forest phenology in the Brazilian Amazon: Evidence from MODIS image time series analysis. *Remote Sensing of Environment* 113(11):2431-2440.
26. Loarie SR, Asner GP, & Field CB (2009) Boosted carbon emissions from Amazon deforestation. *Geophysical Research Letters* 36:L14810.
27. Asner GP, *et al.* (2010) High-resolution forest carbon stocks and emissions in the Amazon. *Proceedings of the National Academy of Sciences* 107:16738-16742.
28. Huang C-y, Asner GP, Barger NN, Neff JC, & Floyd ML (2010) Regional aboveground live carbon losses due to drought-induced tree dieback in piñon-juniper ecosystems. *Remote Sensing of Environment* 114(7):1471-1479.
29. Asner GP, *et al.* (2011) High-resolution carbon mapping on the million-hectare Island of Hawaii. *Frontiers in Ecology and the Environment* 9(8):434-439.
30. Asner G, *et al.* (2012) Human and environmental controls over aboveground carbon storage in Madagascar. *Carbon Balance and Management* 7(1):2.
31. Asner GP, *et al.* (2012) High-resolution mapping of forest carbon stocks in the Colombian Amazon. *Biogeosciences* 9(7):2683-2696.
32. Carvalho ALd, *et al.* (2013) Bamboo-Dominated Forests of the Southwest Amazon: Detection, Spatial Extent, Life Cycle Length and Flowering Waves. *PLoS ONE* 8(1):e54852.
33. Nelson BW, *et al.* (1994) Forest disturbance by large blowdowns in the Brazilian Amazon. *Ecology* 75(3):853-858.
34. Asner GP, Keller M, Pereira R, Zweede JC, & Silva JNM (2004) Canopy damage and recovery after selective logging in Amazonia: Field and satellite studies. *Ecological Applications* 14(4, Suppl. S):S280-S298.
35. Asner GP, *et al.* (2005) Selective logging in the Brazilian Amazon. *Science* 310:480-482.
36. Broadbent EN, *et al.* (2008) Forest fragmentation and edge effects from deforestation and selective logging in the Brazilian Amazon. *Biological Conservation* 141:1745-1757.
37. Bryan JE, *et al.* (2013) Extreme differences in forest degradation in Borneo: comparing practices in Sarawak, Sabah, and Brunei. *PLoS ONE* 8(7):e69679.
38. Souza C, Firestone L, Silva LM, & Roberts D (2003) Mapping forest degradation in the Eastern Amazon from SPOT 4 through spectral mixture models. *Remote Sensing of Environment* 87(4):494-506.
39. Souza C, Roberts DA, & Cochrane MA (2005) Combining spectral and spatial information to map canopy damages from selective logging and forest fires. *Remote Sensing of Environment* 98:329-343.
40. Asner GP (2014) Satellites and psychology for improved forest monitoring. *Proceedings of the National Academy of Sciences* 111(2):567-568.
41. Asner GP (2009) Tropical forest carbon assessment: integrating satellite and airborne mapping approaches. *Environmental Research Letters* 3:1748-9326.
42. Asner G, *et al.* (2013) High-fidelity national carbon mapping for resource management and REDD+. *Carbon Balance and Management* 8(1):7.
43. Asner GP, *et al.* (2012) A universal airborne LiDAR approach for tropical forest carbon mapping. *Oecologia* 168(4):1147-1160.
44. Asner GP & Mascaro J (2014) Mapping tropical forest carbon: Calibrating plot estimates to a simple LiDAR metric. *Remote Sensing of Environment* 140(0):614-624.
45. Zolkos SG, Goetz SJ, & Dubayah R (2013) A meta-analysis of terrestrial aboveground biomass estimation using lidar remote sensing. *Remote Sensing of Environment* 128:289-298.
46. Rejou-Mechain M, *et al.* (2014) Local spatial structure of forest biomass and its consequences for remote sensing of carbon stocks. *Biogeosciences Discuss.* 11(4):5711-5742.

47. Danae M & Mollicone D (2010) Options for sampling and stratification for national forest inventories to implement REDD+ under the UNFCCC. *Carbon Balance and Management* 5:1-9.
48. Mascaro J, *et al.* (2014) A tale of two "forests": Random Forest machine learning aids tropical forest carbon mapping. *PLoS ONE* 9(1):e85993.
49. Baccini A & Asner GP (2013) Improving pantropical forest carbon maps with airborne LiDAR sampling. *Carbon Management* 4(6):591-600.
50. INGEMMET (2000) Mapa Geologico del Peru. (Instituto Geologico Minero y Metalurgico, Lima).
51. Rebata LA, Gingras MK, Räsänen ME, & Barberi M (2006) Tidal-channel deposits on a delta plain from the Upper Miocene Nauta Formation, Marañon Foreland Sub-basin, Peru. *Sedimentology* 53(5):971-1013.
52. Higgins MA, *et al.* (2011) Geological control of floristic composition in Amazonian forests. *Journal of Biogeography* 38(11):2136-2149.
53. Higgins MA, *et al.* (2012) Use of Landsat and SRTM Data to Detect Broad-Scale Biodiversity Patterns in Northwestern Amazonia. *Remote Sensing* 4(8):2401-2418.
54. Räsänen M, Neller R, Salo J, & Jungner H (1992) Recent and Ancient Fluvial Deposition Systems in the Amazonian Foreland Basin, Peru. *Geological Magazine* 129(3):293-306.
55. Espurt N, *et al.* (2010) The Nazca Ridge and uplift of the Fitzcarrald Arch: implications for regional geology in northern South America. *Amazonia, Landscape and Species Evolution: A Look into the Past*, eds Hoorn C & Wesselingh FP (Wiley-Blackwell, New York).
56. Ruokolainen K, Tuomisto H, Macia MJ, Higgins MA, & Yli-Halla M (2007) Are floristic and edaphic patterns in Amazonian rain forests congruent for trees, pteridophytes and Melastomataceae? *Journal of Tropical Ecology* 23:13-25.
57. MINAM (2012) Memoria Técnica de la Cuantificación de los Cambios de la Cobertura de Bosque y Deforestación en el Ambito de la Amazonía Peruana (Periodo 2009-2010-2011). (Peruvian Ministry of Environment, Lima, Peru), p 62.
58. Asner GP, *et al.* (2012) Carnegie Airborne Observatory-2: Increasing science data dimensionality via high-fidelity multi-sensor fusion. *Remote Sensing of Environment* 124(0):454-465.
59. Asner GP, Hughes RF, Varga TA, Knapp DE, & Kennedy-Bowdoin T (2009) Environmental and biotic controls over aboveground biomass throughout a tropical rain forest. *Ecosystems* 12:261-278.
60. Taylor PG, *et al.* (in press) Landscape-scale controls on aboveground forest carbon stocks on the Osa Peninsula, Costa Rica.
61. Mascaro J, Detto M, Asner GP, & Muller-Landau HC (2011) Evaluating uncertainty in mapping forest carbon with airborne LiDAR. *Remote Sensing of Environment* 115(12):3770-3774.
62. Brown S, Gillespie AJR, & Lugo AE (1989) Biomass estimation methods for tropical forests with application to forest inventory. *Forest Science* 35:881-902.
63. Lowell K (1996) Discrete polygons or a continuous surface: which is the appropriate way to model forests cartographically? *Spatial Accuracy Assessment in Natural Resources and Environmental Sciences: 2nd International Symposium*, eds Mowrer HT, Czaplowski RL, & Hamre RH (U.S. Department of Agriculture, Forest Service, Rocky Mountain Forest and Range Experiment Station, Fort Collins, Colorado), pp 235-242.
64. USDA Forest Service (2008) Forest Inventory and Analysis Program. (USDA, Arlington, VA).
65. McRoberts RE, Næsset E, & Gobakken T (2013) Inference for lidar-assisted estimation of forest growing stock volume. *Remote Sensing of Environment* 128:268-275.
66. Breiman L (2001) Random forests. *Machine Learning* 45:5-32.
67. Evans JS, Murphy MA, Holden ZA, & Cushman SA (2011) Modeling species distribution and change using random forest. *Predictive species and habitat modeling in landscape ecology: concepts and applications*, eds Drew CA, Wiersma YF, & Huettmann F (Springer Science, New York, NY), pp 139-159.
68. Cimmery V (2010) User Guide for SAGA (version 2.0.5) (SourceForge).
69. LPDAAC (2011) MOD09A1. ed Center NLPDAA (USGS Earth Resources Observation and Science (EROS), Sioux Falls, SD USA).
70. Mascaro J, Litton CM, Hughes FR, Uowolo A, & Schnitzer SA (2011) Minimizing bias in biomass allometry: model selection and log-transformation of data. *Biotropica* 43(6):649-653.
71. Malhi Y, *et al.* (2010) Introduction: Elevation gradients in the tropics: laboratories for ecosystem ecology and global change research. *Global Change Biology* 16(12):3171-3175.

72. Peacock J, Baker TR, Lewis SL, Lopez-Gonzalez G, & Phillips OL (2007) The RAINFOR database: monitoring forest biomass and dynamics. *Journal of Vegetation Science* 18(4):535-542.
73. Girardin CAJ, *et al.* (2013) Comparison of biomass and structure in various elevation gradients in the Andes. *Plant Ecology and Diversity* 6(3):100-110.



Examples of Peruvian ecosystems mapped in 3-D by the Carnegie Airborne Observatory



ISBN: 978-0-9913870-7-6



9 780991 387076